Published in final edited form as:

Nature. 2018 July ; 559(7712): 61–66. doi:10.1038/s41586-018-0237-5.

Nuclear Arp2/3 drives DNA break clustering for homology-directed repair

Benjamin R. Schrank[1], **Tomas Aparicio**[1], **Yinyin Li**[5], **Wakam Chang**[4], **Brian T. Chait**[5], **Gregg G. Gundersen**[4], **Max E. Gottesman**[2], and **Jean Gautier**[1,3]

[1]Institute for Cancer Genetics, College of Physicians and Surgeons, Columbia University, New York, NY 10032, USA

[2]Department of Biochemistry and Biophysics, College of Physicians and Surgeons, Columbia University, New York, NY 10032, USA

[3]Department of Genetics and Development, College of Physicians and Surgeons, Columbia University, New York, NY 10032, USA

[4]Department of Pathology and Cell Biology, College of Physicians and Surgeons, Columbia University, New York, NY 10032, USA

[5]Laboratory of Mass Spectrometry and Gaseous Ion Chemistry, The Rockefeller University, New York, NY 10065

Abstract

DNA double-strand breaks (DSBs) repaired by non-homologous end joining (NHEJ) display limited DNA end processing and chromosomal mobility. In contrast, DSBs undergoing homology-directed repair (HDR) exhibit extensive processing and enhanced motion. The molecular basis for this movement is unknown. Using *Xenopus laevis* cell-free extracts and mammalian cells, we establish that nuclear actin, WASP and the Arp2/3 complex are recruited to damaged chromatin undergoing HDR. We demonstrate that nuclear actin polymerization is required for the migration of a subset of DSBs into discrete sub-nuclear clusters. Actin-driven movements specifically affect DSBs repaired by HDR in G2; inhibition of actin nucleation impairs DNA end-processing and HDR efficiency. In contrast, Arp2/3 is not enriched at DSBs repaired by NHEJ and does not regulate NHEJ. Our findings establish that nuclear actin-based mobility shapes chromatin organization by generating repair domains essential for HDR in eukaryotic cells.

DSBs induce chromatin movement. In budding yeast, which repair DSBs primarily by HDR, induction of a single chromosomal break triggers increased local mobility: the DSB mean-

AUTHOR FOR CORRESPONDENCE: jg130@cumc.columbia.edu.
Correspondence and requests for materials should be addressed to J.G. (jg130@cumc.columbia.edu)

The authors declare no competing financial interests

AUTHOR CONTRIBUTIONS: J.G. and B.R.S conceived the study and wrote the manuscript. B.R.S. conducted the majority of the experiments and data analyses. T.A. and Y.L. performed the mass spectrometry experiments. G.G.G., M.E.G., W.C., B.T.C., T.A. and Y.L. assisted with data analysis and interpretation.

square displacement is significantly higher than that of an undamaged region[1,2]. Moreover, multiple DSBs cluster after traversing long distances[3]. DSB clustering may facilitate homology search, increase repair efficiency or shield breaks from misrepair[4,5]. These movements are intricately related to HDR. Factors critical for resection initiation and downstream recombination are essential for DSB mobility in yeast[1,2]. In mammalian cells, DSBs are often described as more stable suggesting that NHEJ, the predominant repair pathway, limits movement[6–8]. However, in HeLa cells, Rad51-positive DSBs induced by alpha particles cluster[4]. Similarly, damaged telomeres in U2OS cells that are maintained by recombination merge in a Rad51-dependent manner[9]. Moreover, damaged active genes cluster in preparation for HDR[5]. Deprotected mouse telomere movements require the LINC complex which transmits cytoskeletal forces from the cytoplasm[10]. The molecular basis for DSB movement and its role in DNA repair, however, remain enigmatic.

The machinery that drives actin polymerization in the cytoplasm is also found in the nucleus[11]. Specifically, the Arp2/3 complex as well as its activator WASP, a Wiskott-Aldrich syndrome family member, are located in both cellular compartments[12–14]. WASP brings the Arp2 and Arp3 subunits into close proximity to activate the complex and enable filament elongation[15]. Genotoxic agents trigger actin polymerization in the nucleoplasm of mammalian cells[16]; however, actin polymerization's role in DSB repair is not characterized.

Actin nucleators bind damaged chromatin

We performed an unbiased proteomics screen to document the recruitment of proteins to chromosomal DSBs in cell-free S-phase extracts derived from *Xenopus* eggs. Peptides from control or DSB-containing chromatin protein fractions were labeled with isobaric tags and subjected to liquid chromatography mass spectrometry. We observed enrichment of known DSB repair regulators and proteins not previously associated with the DNA damage response (Extended Data Fig. 1a). Among such proteins were all seven subunits of the actin nucleating complex Arp2/3, as well as β-actin and capping proteins (Extended Data Fig. 1a). We confirmed that β-actin, Arpc4, and CapZβ are recruited to Mre11-enriched, DSB-containing chromatin by Western blot (Fig. 1a). We next asked whether actin enrichment at chromosomal DSBs required DNA damage signaling. Inhibition of the PI3K-like kinases ATM and ATR reduced the binding of actin complexes to damaged chromatin (Extended Data Fig. 1b, c). Moreover, treatment with the small molecule inhibitor CK-666, which stabilizes the Arp2/3 complex in an open, inactive conformation[17,18], decreased Arpc4, β-actin, and CapZβ enrichment in damaged chromatin (Fig. 1a, b). Overall, these results reveal that PI3K-like kinases and the Arp2/3 complex regulate the assembly of polymerized actin at chromosomal DSBs in *Xenopus* extracts.

WASP and Arp2/3 bind DSBs undergoing HDR

We next tested whether WASP, an Arp2/3 activator, localized to DSB foci in mammalian cells. DSB generation by Neocarzinostatin (NCS), a radiomimetic antibiotic, induced WASP foci in U2OS cells (Fig. 2a, b). Moreover, WASP significantly co-localized with γH2AX, which marks large chromatin domains surrounding DSBs[19], suggesting that sites of DNA

repair contain WASP (Fig. 2c). Similarly, WASP foci arose in mouse-tail fibroblasts (MTFs) post DSB generation and co-localized with γH2AX (Extended Data Fig. 1d–f).

We next asked whether actin complexes are recruited in close proximity to DSBs. Accordingly, we performed chromatin immunoprecipitation (ChIP) experiments in U2OS cells in which genome-wide DSBs are generated via nuclear translocation of the AsiSI restriction enzyme[20]. We interrogated four DSB sites, annotated DSBs I-IV, in the G1- or G2-phase of the cell cycle in synchronized cells (Fig. 2d). First, we monitored the recruitment of Rad51 and the catalytic subunit of DNA-PK (DNA-PKcs). Rad51 was previously shown to localize to a subset of these DSBs[20]. DNA-PKcs was recruited to all four DSBs in both cell-cycle phases (Fig. 2e). In contrast, we confirmed Rad51 binds exclusively DSBs I and II, which occurs more robustly in G2- than in G1-synchronized cells (Fig. 2f). Taken together, these results demonstrate that HDR may be monitored at a subset of DSBs in G2 and distinguished from DSBs undergoing NHEJ, the more frequent mode of repair.

We then asked if actin filament nucleators localize to DSB sites. WASP accumulated at DSBs I and II in both cell cycle phases (Fig. 2g), whereas Arpc2 recruitment was restricted to G2 (Fig. 2h). Notably, WASP was also enriched at DSBs III and IV whereas Arpc2 was not (Fig. 2g, h). Neither WASP nor Arpc2 were enriched at an undamaged site (Fig. 2i). Collectively, these data establish that WASP binds DSBs independently of repair pathway choice but specifically activates Arp2/3 at DSBs undergoing HDR. This supports a model by which actin polymerization is primed at all DSBs but only triggered during the assembly of HDR machinery.

Arp2/3 inactivation impairs DSB movement

The Arp2/3 complex generates propulsive forces by nucleating a highly-branched network of actin filaments. Since WASP and Arp2/3 localized to Rad51-bound DSBs, we asked whether their activity induces movement and clustering of HDR machinery. Accordingly, we visualized DSB movements using a U2OS cell line that stably expresses Rad52 tagged with mCherry and 53BP1 tagged with YFP[23]. Rad52 mediates recombination and forms foci in S/G2 cells exclusively[21,22]. Generation of DSBs in S/G2 cells yielded robust induction of Rad52-mCherry foci (Fig. 3a). Strikingly, Rad52 foci clustered and merged over a 60-minute interval (Fig. 3a, b and SI Videos 1a–d). Coalescing foci increased in intensity and size and remained merged for a minimum of 15 min (Fig. 3b, c). Notably, Arp2/3 inactivation following treatment with CK-666 decreased the frequency of clustering events and abrogated the increase in foci size (Fig. 3c, d and SI Videos 1e, f). We subsequently compared DSB movements in the presence of CK-666 and CK-689, an inactive control analog[18]. Quantitative analysis of DSB tracks in CK-689-treated cells indicated that Rad52 foci explore a mean cumulative distance of 4.1 μm over 100 min (Fig. 3e, f). Mean-square displacement (MSD) analysis of Rad52 foci revealed a diffusion coefficient $D(t)$ of 3.7×10^{-5} $\mu m^2/s$ (Fig. 3g and Extended Data Fig. 2a). Motion type analysis was consistent with confined Brownian motion. Critically, Arp2/3 inhibition diminished the distance DSBs traveled over the 100-minute period (Fig. 3e, f). Furthermore, CK-666 treatment decreased the Rad52 diffusion coefficient from 3.7 to 1.8×10^{-5} $\mu m^2/s$ (Fig. 3g).

We subsequently monitored DSBs bound by RPA in MTFs expressing RPA32-pEGFP-NLS. Similar to the behavior of Rad52-mCherry foci, RPA32 foci frequently merged over a 60-minute interval (Fig. 3h and SI Videos 1g, h). Notably, CK-666 treatment diminished the distance RPA foci traveled relative to CK-689 (Fig. 3i). Moreover, the diffusion coefficient calculated for RPA foci in cells treated with CK-666 decreased from 4.1 to 2.1×10^{-5} $\mu m^2/s$ (Extended Data Fig. 2a). Finally, we employed MTF cells harboring a conditional Arpc2 allele[23]. Upon 4-OHT treatment, cells are depleted of Arpc2[23] (Fig. 3j). Consistent with CK-666 treatment, RPA movements were significantly attenuated upon Arcp2 depletion (Fig. 3i–l). CK-689 minimally affected Rad52 and RPA foci movement relative to DMSO (Extended Data Fig. 2a, b).

Formation of Rad51 filaments requires ssDNA-RPA intermediates. Thus, we assessed how Arp2/3 inactivation impacts Rad51 foci behavior. To circumvent the lack of a functional fluorescent Rad51 reporter, we employed the Icy bioimaging software and its spatial analysis plug-in (http://www.icy.bioimageanalysis.org) to assess Rad51 foci clustering. This approach was validated in a study showing ATM-dependent clustering of γH2AX foci in fixed cells[24]. Analysis with Icy software revealed that Rad51 foci are highly clustered in the nucleus and that CK-666 reduces this clustering (Extended Data Fig. 3a–d). CK-666 treatment did not affect cell viability, cell cycle progression, nuclear size, nuclear morphology, nor RPA or Rad51 protein expression (Extended Data Fig. 4a–g). These experiments demonstrate that Arp2/3-mediated actin polymerization enhances DSB motion during HDR, thereby increasing the incidence of foci clustering.

In G1 cells, 53BP1 forms foci and regulates end-joining events. Consistent with the lack of Arp2/3 at DSBs in G1 cells (Fig. 2), 53BP1-YFP foci movements in G1 cells were unaffected by Arp2/3 inhibition (Extended Data Fig. 5a–c and Extended Data Fig. 2a). In G2 cells, many 53BP1-YFP and Rad52 foci colocalized, consistent with the localization of 53BP1 at sites of DSB resection[22] (Extended Data Fig. 5d). Relative to G1 cells, the diffusion coefficient for 53BP1 foci increased from 2.4 to 3.5×10^{-5} $\mu m^2/s$ in G2 cells (Extended Data Fig. 5e, f). In contrast to G1 cells, the motion of 53BP1 foci in G2 cells was reduced by Arp2/3 inactivation (Extended Data Fig. 5g). Collectively, these data indicate that Arp2/3 enhances the motion of sites of DSB resection in G2 cells.

Arp2/3 nucleates actin foci at sites of HDR

Genotoxic agents induce nuclear actin structures in mammalian cells[16]. In U2OS cells transfected with nuclear-actin-chromobody-tag-GFP[25], we identified a subset of actin structures resembling foci (actin-cb foci) that increased following NCS treatment (Fig. 4a, b and Extended Data Fig. 6a, b). We also identified brighter, rod-like filaments (Extended Data Fig. 6a, b). Strikingly, actin-cb foci clustered and merged over a 20-minute interval (Fig. 4c and SI Videos 2a, b). MSD analysis of actin-cb foci revealed a $D(t)$ of 3.4×10^{-4} $\mu m^2/s$ (Fig. 4d, e). Similar to Rad52 and RPA, the α coefficient for actin-cb foci indicated confined motion. Notably, CK-666 abolished actin-cb foci, strongly suggesting these structures are sites of Arp2/3-dependent nucleation (Fig. 4f, g, SI Videos 2c–e, and Extended Data Fig. 6d). In contrast, nuclear actin rods exhibited limited mobility and were unaffected by CK-666 (Extended Data Fig. 6a–d). Finally, we compared the localization of actin-cb foci

with Rad51 foci in fixed cells and RPA-mCherry foci using live cell imaging. Following NCS treatment, 46% of Rad51 foci overlapped or abutted actin-cb foci (Fig. 4h). Moreover, we observed co-localization of actin-cb foci and RPA32-mCherry foci, which travelled together in the nucleoplasm (Fig. 4i and Extended Data Fig. 6e, f). Collectively, these experiments provide direct evidence that Arp2/3 assembles dynamic nuclear actin structures at sites of HDR.

WASP and Arp2/3 mediate HDR, not NHEJ

To determine how DSB clustering impacts DNA repair pathways, we utilized a panel of U2OS cell lines that monitor the repair of I-SceI-induced DSBs by HDR, NHEJ, single-strand annealing (SSA), and microhomology-mediated end joining (MMEJ)[26]. Arp2/3 inactivation by CK-666 or CK-548 reduced the ability of cells to repair I-SceI-induced DSBs by HDR or SSA by 40 percent (Fig. 5a, b and Extended Data Fig. 7a, e). Similarly, wiskostatin, a small molecule inhibitor of WASP[27], reduced HDR and SSA efficiency (Fig. 5a, b). Comparable HDR defects in cells depleted of WASP by RNA interference were also observed (Extended Data Fig. 7b–d). Notably, inhibition of WASP or Arp2/3 did not compromise MMEJ or NHEJ, neither of which require significant resection (Fig. 5c, d and Extended Data Fig. 7f, g). Finally, the application of CK-689 did not reduce the repair of I-SceI-induced DSBs by HDR, SSA or NHEJ (Extended Data Fig. 7h).

Although the Arp2/3 complex is found in the nucleus[14], it also polymerizes actin in the cytoplasm. To strengthen the idea that the HDR defect was a direct consequence of inhibiting nuclear actin polymerization, we increased nuclear actin levels by overexpressing actin fused to a nuclear localization sequence (WT-actin-NLS) (Fig. 5e). Whereas expression of WT-actin-NLS did not affect HDR, overexpression of an actin variant that interrupts filament formation (R62D-actin-NLS) significantly inhibited HDR to levels comparable with Arp2/3 inhibition (Fig. 5f). Treatment of cells expressing R62D-actin-NLS with CK-666 did not further reduce HDR, suggesting that nuclear actin and Arp2/3 functioned together. Moreover, WT-actin, R62D-actin, and WT-actin-NLS tagged with mCherry did not affect DSB repair, whereas expression of R62D-actin-NLS significantly inhibited HDR (Extended Data Fig. 8a, b). This strongly suggests that inhibiting actin polymerization in the cytoplasm does not influence DNA repair in the nucleus. Similar to CK-666, expression of R62D-actin-NLS did not reduce NHEJ-based repair (Fig. 5g). Finally, neither siRNA directed against the actin filament nucleator formin-2 nor treatment with the formin inhibitor SMIFH2 inhibited HDR efficiency (Extended Data Fig. 8c–f). This observation thus demonstrates the specific requirement for Arp2/3 complex activity in HDR.

Arp2/3 activity enhances DSB resection

To assess the functional significance of Arp2/3-driven DSB mobility, we compared the repair kinetics of two AsiSI-induced DSB sites (DSBs V, VI) that undergo up to 3.5 kb of resection[24]. In G1 cells, the repair kinetics of both DSBs were identical in the presence or absence of CK-666, confirming that Arp2/3 does not influence NHEJ (Fig. 6a). In contrast, in G2 cells, CK-666 substantially slowed repair at the two DSB sites interrogated (Fig. 6b).

To address how actin-driven clustering might promote HDR efficiency, we asked if the Arp2/3 complex facilitates resection. Arp2/3 complex inactivation decreased ssDNA generation at DSBs V and VI by 50 percent, indicating that clustering facilitates DSB end-resection (Fig. 6c). We consolidated this finding by quantifying Rad51 foci that arise following DSB resection in NCS-treated cells over 24 hours (Fig. 6d, e). In control cells, the number of Rad51 foci first increased from 2 to 8 hours then decreased up to 24 hours, indicative of recruitment and repair (Fig. 6d). In contrast, Rad51 foci minimally increased following Arp2/3 inhibition (Fig. 6d, e). Moreover, substantially fewer Rad51 foci arose in Arpc2-depleted MTFs (Fig. 6f, g).

In yeast and human cells, DSB motion requires the HDR machinery[1,2,5]. We wondered whether Rad52 movement requires MRN complex activity[28]. Accordingly, we treated U2OS cells with mirin, a small molecule inhibitor that abolishes the nuclease activity of Mre11[29]. Mirin lowered ssDNA levels at DSBs V and VI by 70% (Fig. 6h). Notably, mirin significantly decreased the D(t) of Rad52 foci from 4.4 to 2.4×10^{-5} $\mu m^2/s$ (Fig. 6i and Extended Data Fig. 2a) but did not significantly affect the MSD of 53BP1 foci in G1 cells (Fig. 6j.) Taken together, these observations suggest a positive feedback loop, wherein resection enhances DSB movements, which in turn, enhance resection.

Wiskott–Aldrich syndrome (WAS) is an X-linked disorder characterized by severe immunodeficiency and predisposition to non-Hodgkin's lymphoma and leukemia[30]. Given that inactivation of WASP by Wiskostatin or siRNA produced defects in HDR (Fig. 5a and Extended Data Fig. 7d), we tested B-lymphocytes derived from WAS patients for defects in DSB end-resection. Relative to lymphocytes derived from healthy individuals, lymphocytes bearing two distinct WAS mutations exhibited fifty percent fewer RPA-positive cells upon camptothecin (CPT) exposure, consistent with a resection defect (Fig. 6k and Extended Data Fig. 9a–d). Moreover, WAS mutant cells were more sensitive to CPT treatment than healthy lymphocytes (Extended Data Fig. 10a, b). Arp2/3 inhibition by CK-666 also enhanced CPT-induced lethality in U2OS cells (Extended Data Fig. 10c). Finally, Arp2/3 inhibition sensitized cells to aphidicolin and the PARP1 inhibitor olaparib, indicating a reduced tolerance to replication stress (Extended Data Fig. 10d, e). Taken together, these experiments demonstrate that Arp2/3 activation by WASP enhances the processing and resolution of DSBs undergoing HDR.

Discussion

DSB mobility is influenced by cell cycle stage, chromatin state, and repair pathway choice. Our finding that Arp2/3 specifically enhances the movement of HDR breaks is supported by studies showing that DSB mobility requires DNA end-resection. In S/G2, DSBs induced in pericentric heterochromatin relocate to the nuclear periphery, whereas DSBs generated in G1 remain stable[31]. Critically, blocking HDR or resection prevented DSB mobility in G2. Similarly, in Drosophila, the activities of CtIP, Exo1, and Blm were necessary for DSB movement outside the heterochromatic domain[32]. Conversely, we now show Arp2/3 inhibition decreases end processing, consistent with positive feedback regulation between DSB mobility and resection. Indeed, DSB clustering could facilitate enzymatic reactions by increasing the local concentration of repair factors. Interestingly, in budding yeast, Arp2,

Arp3, and Arpc2 are synthetic lethal in combination with Mre11 or Sgs1 deficiency[33]. This supports actin polymerization and resection interdependency.

Our ChIP analyses suggest a two-step mechanism for actin nucleation at HDR sites (Extended Data Fig. 10f). WASP is recruited at all DSBs regardless of cell cycle stage, reminiscent of NHEJ factors. In contrast, Arp2/3 is recruited in G2 to breaks that assemble HDR machinery. Actin polymerization promoted by WASP and Arp2/3 might therefore require sequential activation of PI3K-like kinases. Whereas ATM promotes the assembly of complexes required for resection, ATR commits repair to HDR[28]. Accordingly, following ATM activation and WASP recruitment at DSBs, resection initiation could create a permissive environment for Arp2/3 activity leading to increased chromosomal mobility at specific DSB sites.

METHODS

Chromatin binding assay and western blot

Preparation of Low-Speed Supernatant (LSS) *Xenopus* egg extracts and isolation of demembranated sperm nuclei (chromatin) were performed as previously described [34]. For chromatin binding experiments, 15 μl of LSS extracts were supplemented with demembranated sperm nuclei (2,500 sperm/μl) and incubated for 10 min at 21ºC before addition of DMSO or one of the following compounds for 10 min: CK-666 (160 μM), CK-548 (160 μM) KU5593 (100 μM), VE821 (50 μM). Subsequently, the PflMI restriction endonuclease was added to each sample (0.05U/μl) before incubation for an additional 60 min at 21ºC. Extracts were diluted in chromatin isolation buffer (50 mM Hepes-KOH, pH 7.8, 100 mM KCl, 2.5 mM $MgCl_2$) supplemented with 0.125% Triton X-100 and overlaid on top of sucrose cushions (chromatin isolation buffer plus 30% sucrose) in 1.5 ml low-retention tubes (Thermo Fisher Scientific). Samples were spun at 7180 RPM for 30 min at 4ºC in a swing-bucket Sorval rotor (HB-6). Chromatin pellets were resuspended in 10 μl Laemmli buffer, boiled, and fractionated on a 4 – 22% Tris-Glycine gel (Invitrogen) according to standard procedures, followed by transfer of resolved proteins onto PVDF membranes. Following a 1 hr block with 5% milk, membranes were incubated overnight at 4ºC with one of the following primary antibodies against: β-actin (Sigma Aldrich: A5316, 1/1000), Arpc4 (Novus Biologicals: NBP1-69003, 1/500), Capping protein β-2 subunit (Developmental Studies Hybridoma Bank: E00007, 1/10000), Histone H3 (Cell Signaling Technology, 9715, 1/2000) and Xenopus Mre11 [34]. HRP-conjugated secondary antibodies were used (Anti-Rabbit IgG HRP, Anti-Mouse IgG HRP, Fisher Scientific) and chemiluminescence (Supersignal West Pico Chemiluminescent Substrate, 34077) was used.

Mass spectrometric analysis of DSB-containing chromatin

Chromatin samples were isolated as described above with the following modifications: 100μl of LSS extracts were supplemented with sperm nuclei (5,000 sperm/μl) and incubated for 10 min at 21ºC before addition of PflMI restriction endonuclease (0.05U/μl) and incubated for an additional 60 min. Chromatin was isolated through sucrose cushions as described above and extensively digested with 100U of micrococcal nuclease for 30 min at 37ºC (NEB). Chromatin proteins were reduced with DTT (5mM, 30 min 60ºC) and alkylated

with iodoacetamide (15mM, 30 min RT) before fractionation on SDS-PAGE. “in-gel” digestion was performed with proteomic-grade trypsin (Promega) at 5 ng/μl for 16 hrs at 37ºC. The resulting digestion peptides were extracted from the gel pieces with 1:2 (vol/vol) 5% formic acid: acetonitrile solution. The resulting peptides were labeled with isobaric mass tags (ITRAQ 4-plex, Sciex), combined, purified with in-house made STAGE tips [35], resuspended in 0.5% acetic acid and loaded onto a home-packed reverse phase C18 column (75 μm I.D.). The peptides were separated using a linear gradient (0 % to 42 % acetonitrile, 0.5 % acetic acid, 120 min, 150 nL/min) and directly sprayed into an LTQ-Orbitrap-Velos mass spectrometer for analysis (Thermo). The repetitive analytical cycle incorporated a high-resolution mass scan in the Orbitrap (resolution = 30,000) followed by tandem MS scans of the five most intense peaks observed in each Orbitrap mass spectrum. Peptides were identified and quantified using Proteome Discoverer software (Thermo, Version 1.4).

Cell culture and drug treatment

U2OS and mouse-tail fibroblast cell lines were cultured in high-glucose Dulbecco’s modification of Eagles media supplemented with L-Glutamine, 10% fetal bovine serum, and 1% penicillin-streptomycin. For Neocarzinostatin-dependent DSB induction, cells were cultured on 8-well chamber slides (Thermo Fisher Scientific) and were treated with 0.5 μg/ml NCS for 60 min at 37 °C. Cells were washed twice with PBS before adding media containing DMSO or one of the following compounds: CK-666 (Sigma Aldrich: SML-006, 100 μM), CK-548 (Sigma Aldrich: C7499, 50 μM), CK-689 (Sigma Aldrich: 18251750, 100 μM), and Wiskostatin (Sigma Aldrich: W2270, 3 μM). After drug treatment, cells were then incubated at 37 °C for the indicated times. For mirin experiments, cells were pre-treated with mirin (Sigma Aldrich: M9948, 50 μM) for 1 hour, prior to addition of NCS,

ER-AsiSI U2OS cells stably expressing the AsiSI restriction endonuclease tethered to the estrogen receptor were generously provided by Dr. G. Legube, Centre de Biologie Integrative – Toulouse. For cell synchronization, cells were treated with 2 mM thymidine for two 18 hr intervals separated by an 11 hr release in fresh media. Cells underwent double-thymidine block and were released into fresh media for 7 hrs (G2) or 15 hrs (G1) prior to AsiSI-dependent DSB induction with media supplemented with 300 nM 4OHT (Sigma Aldrich, H7904) plus CK-666, CK-548, wiskostatin, or DMSO. Cells were subsequently incubated at 37 °C for 4 h.

Arpc2$^{-/-}$ fibroblast cell lines (generously provided by Dr. J.E. Bear, University of North Carolina) stably express the Cre-recombinase tagged to the estrogen receptor. Upon 4-OHT treatment, the Arpc2 locus is floxed by Cre and cells are depleted of Arpc2 following 4 days of 4-OHT treatment.

CB33 and RD lymphoblastoid B-cell lines were a kind gift of Dr. Riccardo Dalla-Favera (Columbia University). Two B-lymphocyte cell lines bearing distinct mutations in the gene WAS were obtained from the NIGMS Human Genetic Cell Repository (Coriell: GM1267, GM1268). GM1267 harbors a G>A transition at position 4 in intron 6 of the WAS gene (IVS6+5G>A). This mutation activates a cryptic splice site leading to splicing of a 38-nucleotide sequence from intron 6 onto exon 7. GM1268 harbors a G>A transition at nucleotide 257 in exon 2 on the WAS gene. This mutation results in a methionine for valine

substitution at codon 75 (V75M). All B-cell lines were grown in Rosewell Park Memorial Institute Medium with 20% heat-inactivated bovine serum with 2mM L-glutamine added.

Immunohistochemistry and quantification of DSB repair protein foci

U2OS cells were cultured on 8-well chamber slides (Thermo Fisher Scientific) and subjected to drug treatments as described above. Cells were then washed once with PBS before fixation with freshly-prepared 4% PFA (pH 7.4) for 10 min. Cells were subsequently washed twice with PBS for 10 min prior to permeabilization with 0.1% PBS-Triton X-100 for 10 min. Cells were then washed once with PBS for 5 min before incubation with blocking buffer (3% BSA in 0.2% PBS-Tween) for 1 h. Cells were stained with primary antibodies diluted in blocking buffer under a Hybrislip (Invitrogen) overnight in a humidified chamber at 4°C. Primary antibodies include γH2AX (EMD Millipore: 05-636, 1/500 or Abcam: ab81299, 1/500), WASP (Santa Cruz: sc-5300, 1/50), Rad51 (Santa Cruz: sc-8349, 1/50), 53BP1 (Novus Biologicals: NC100-304, 1/250) and FLAG (Sigma Aldrich: F3165, 1/250). Cells were then washed three times in PBS for 15 min and incubated with a fluorescent-conjugated secondary antibody in PBS with DAPI (Invitrogen, 1/10000) for 1 hr at room temperature. Secondary antibodies were Alexa 488 conjugated goat anti-mouse Ig (Abcam: ab150113, 1/1000), Alexa 488 conjugated goat anti-rabbit Ig (Thermo Fisher Scientific, A-11034, 1/10000), and Alexa 594 conjugated goat anti-mouse Ig (Thermo Fisher Scientific, A-11005, 1/10000). Cells were then washed three times with PBS for 15 min. Vectashield was applied to each slide and slides were coverslipped. Slides were analyzed under 40X magnification using a Zeiss Axio Imager Z2 microscope, equipped with a CoolCube1 camera (Carl Zeiss, Thornwood, NY, USA). Images were processed for contrast enhancement and background reduction using ImageJ.

MetaCyte software (Metasystems, Newton, MA, USA, Version 3.10.6) was used to detect U2OS nuclei based on DAPI staining and perform automated quantification of γH2AX, Rad51, and WASP foci within each nucleus. For foci size and clustering analyses, images were converted to Grayscale and processed with Icy Software (Version 1.8.6.0; Institut Pasteur, Quantitative Image Analysis Unit; http://www.icy.bioimageanalysis.org). Regions of interest were drawn around individual nuclei and foci were detected using the Spot Detector plug-in (Channel 0) [36]. For clustering analyses, spots detected using Scale 2 (3 px) were exported to the spatial analysis plug-in, which utilizes Ripley's K-function to assess the deviance of pairs of points from total randomness [24,36]. The software reports statistically significant clustering ($p<0.05$) when the K-function crosses the clustering threshold. The software further corrects for the number of points in the computations of the quantiles of the Ripley's K function. Thus, there is no loss of statistical power for samples with lower numbers of foci. For foci size analysis, foci with minimum sizes of 1 px and 3 px were counted using the Spot Detector plug-in. Scale 1 was used to detect foci that were ≥ 1 px in size, whereas Scale 2 was used to detect foci that were ≥ 3 px. Foci that met criteria for Scale 1 (≥ 1 px) and Scale 2 (≥ 3 px) were excluded from the Scale 1 group to avoid duplicate detections. Foci counts were subsequently averaged to determine the mean size of foci per nucleus (100 nuclei were detected per condition or as indicated). For co-localization studies, images were imported into Image J (NIH) and separated into green (γH2AX) and red (WASP) channels. These files were subsequently imported into Icy and regions of

interest were drawn around individual nuclei. Pearson *r* was calculated using the Co-localization Studio plug-in, which compares the coincidence of spots inside a region of interest between green and red channels.

Chromatin immunoprecipitation

ChIP experiments followed previously published protocols with the following modifications [20]: 50 million ER-AsiSI U2OS cells were cultured on 150mm^2 plates in high-glucose Dulbecco's modification of Eagles media supplemented with L-Glutamine, 10% fetal bovine serum, and 1% penicillin-streptomycin. Following double-thymidine block, cells were released into fresh media for 7 hr (G2) or 15 hr (G1) before incubation with 300 nM 4-OHT for 4 h. Cells were then trypsinized, washed with PBS, cross-linked in 1% methanol-free formaldehyde fixing buffer for 10 min, quenched with 0.125M glycine for 5 min, and snap frozen at −80 ºC. Cell lysis and nuclear isolation were performed using NP40 lysis buffer and SDS shearing buffer (Covaris). Nuclei were sonicated using the S220 Ultrasonicator (Covaris) to obtain chromatin fragments of 500 – 1000 bp in length. Sheared chromatin was incubated with 10 μg antibodies to Rad51 (Santa Cruz: sc-8349), DNA-PKcs (Abcam: ab1832), WASP (Santa Cruz: sc-5300), Arpc2 (Santa Cruz: sc-32195) or IgG (Jackson ImmunoResearch Laboratories) overnight. These antibodies were validated for ChIP by previous studies [12,20]. Protein A/G magnetic beads were added overnight, followed by sequential washes at increasing stringency and reverse cross-linking at 65 ºC. Immunoprecipitated DNA and input DNA were analyzed in triplicate by qPCR. ChIP efficiencies (measured as percent of input immunoprecipitated) were measured by qPCR at sites 80 bp downstream of DSBs. Graphs show ChIP efficiencies in G1, G2, or No 4-OHT cells, pooled from three experiments, and normalized against input material. Sequences for primers are listed below: DSB I: 5′-GTCCCTCGAAGGGAGCAC-3′, 5′-CCGACTTTGCTGTGTGACC-3′; DSB II: 5′-CCGCCAGAAAGTTTCCTAGA-3′, 5′-CTCACCCTTGCAGCACTTG-3′; DSB III: 5′-TCCCCTGTTTCTCAGCACTT-3′, 5′-CTTCTGCTGTTCTGCGTCCT-3′; DSB IV: 5′-ATCGGGCCAATCTCAGAGG-3′, 5′-GCGACGCTAACGTTAAAGCA-3′. Primer pairs used to measure Rad51, DNA-PK(cs), WASP, and Arpc2 were located 80 bp from DSB sites or at an undamaged genomic locus.

I-SceI-induced DSB repair assays

U2OS cell lines which harbor chromosomally-integrated I-SceI-based GFP reporter substrates were used to monitor the efficiency of HDR, SSA, MMEJ, and c-NHEJ repair processes. The DR-GFP, SA-GFP, EJ2-GFP, and EJ5-GFP cell lines (generous gifts from Dr. J. Stark, City of Hope Cancer Center) were transfected with 1 μg of I-SceI expressing vector (FuGENE 6 transfection reagent (Promega), Opti-MEM (Gibco)) in the media supplemented with DMSO or one of the following compounds: CK-666 (Sigma Aldrich: SML-006, 50 μM), CK-548 (Sigma Aldrich: C7499, 25 μM), CK-689 (Sigma Aldrich: 18251750 μM), SMIFH2 (Sigma Aldrich: S4826, 5 μM), or wiskostatin (Sigma Aldrich: W2270, 3 μM). The I-SceI expressing vector was a gift of Dr. Richard Baer. For the FLAG actin construct overexpression experiments, DR-GFP cells were transfected with FLAG-WTactin-NLS or FLAG-R62Dactin-NLS for 48 hr prior to transfection with I-SceI in media supplemented with DMSO or CK-666. For the mCherry actin construct overexpression experiments, DR-GFP cells were co-transfected with I-SceI and mCherry-WTactin, mCherry-WTactin-NLS,

mCherry-R62Dactin, or mCherry-R62Dactin-NLS. Cells were harvested 48 hr post I-SceI transfection and % GFP^+ events were counted by FACS (10,000 cells per biological replicate). For all conditions, parallel transfection with 1 μg of pEGFP-N3 vector (Clontech) was used to determine transfection efficiency. Percentage refers to the number of GFP^+ cells divided by the number of pEGFP+ cells.

Resection assay

A detailed protocol for the resection assay has been recently described [37]. Briefly, ER-AsiSI U2OS cells were treated with 300 nM 4-OHT in media supplemented with DMSO, CK-548 (50 μM), or CK-666 (100 μM). For mirin experiments, cells were pre-treated with mirin (Sigma Aldrich: M9948, 50 μM) for 1 hour prior to addition of 4-OHT, and subsequently washed and incubated with mirin for indicated time points. After 4 hours, cells were trypsinized and washed with cold PBS before resuspension in lysis buffer (100 mM NaCl, 10 mM TrisCl pH 8, 25 mM EDTA, pH 8, 0.5% SDS, 0.1 mg/mL proteinase K). Cells were agitated at 37°C overnight. After phenol/chloroform purification and salt/ethanol extraction, precipitated DNA underwent restriction enzyme digest by BamHI-HF, BsrGI, or HindIII-HF (1 unit of enzyme per 7 ng of DNA) at 37 °C overnight. DNA digests were subsequently used as templates in a 20 uL qPCR reaction containing 10.0 μL 2× TaqMan Universal PCR Master mix (Thermo), 0.5 μM of each primer, and 0.2 μM of probe. The extent of ssDNA generation at sites downstream of various DSBs was determined by calculating the ΔCt value for each site (mock-digested Ct value - digest Ct value) and employing the following equation: ssDNA = 1/(2^(ΔCt-1)+0.5)*100. Sequences for primers and probes are listed below: DSB V (335 bp site): 5′-GAATCGGATGTATGCGACTGATC-3′, 5′-TTCCAAAGTTATTCCAACCCGAT-3′; 6FAM-CACAGCTTGCCCATCCTTGCAAACC-TAMRA; DSB V (1618 bp site): 5′-TGAGGAGGTGACATTAGAACTCAGA-3′, 5′-AGGACTCACTTACACGGCCTTT-3′; 6FAM-TTGCAAGGCTGCTTCCTTACCATTCAA-TAMRA; DSB V (3500 bp site): 5′-TCCTAGCCAGATAATAATAGCTATACAAACA-3′, 5′-TGAATAGACAGACAACAGATAAATGAGACA-3′; 6FAM-ACCCTGATCAGCCTTTCCATGGGTTAAG-TAMRA; DSB VI (364 bp site): 5′-CCAGCAGTAAAGGGGAGACAGA-3′, 5′-CTGTTCAATCGTCTGCCCTTC-3′; 6FAM-CCAGGCCCTCAAAATCCCTCCACTG-TAMRA; DSB VI (1754 bp site): 5′-GAAGCCATCCTACTCTTCTCACCT-3′, 5′-GCTGGAGATGATGAAGCCCA-3′; 6FAM-CACTCCCTGTTCTTCTTCTGCTCCCGA-TAMRA; DSB VI (3564 bp site): 5′-GCCCAGCTAAGATCTTCCTTCA-3′, 5′-CTCCTTTGCCCTGAGAAGTGA-3′; 6FAM-CTGCAGCCCTCAAGCCCGGAT-TAMRA. No DSB site: 5′-ATTGGGTATCTGCGTCTAGTGAGG-3′, 5′-GACTCAATTACATCCCTGCAGCT-3′; 6FAM-TCTCTGCACAGACCGGCTTCCCTTC-TAMRA.

AsiSI-AID repair assay

The repair assay followed recently published protocols with the following modifications [20,24]. 5 million ER-AsiSI-AID U2OS cells were cultured on 100mm^2 plates in high-glucose Dulbecco's modification of Eagles media supplemented with L-Glutamine, 10% fetal bovine serum, and 1% penicillin-streptomycin. Following double-thymidine block, cells were released into fresh media for 7 hr (G2) or 15 hr (G1) before incubation with 300 nM 4-OHT

and DMSO or CK-666 (100 μM) for 4 h. Cells were subsequently washed 3 times with PBS and then incubated in media containing auxin (Sigma: I5148, 500 μg/mL) and DMSO or CK-666. Cells were harvested 0, 2, or 8 hr after auxin exposure. Phenol/chloroform purification followed by salt/ethanol extraction was performed to precipitate DNA. DNA were subsequently used as templates in a 20 μL qPCR reaction containing 10.0 μL 2× TaqMan Universal PCR Master mix (Thermo), 0.5 μM of each primer, and 0.2 μM of probe. The level of unrepaired DSBs was determined by normalizing the Ct value for each DSB site with a control, undamaged site. Sequences for primers and probes are listed below. DSB V (Across DSB): 5′-GATGTGGCCAGGGATTGG-3′, 5′-CACTCAAGCCCAACCCGT-3′; DSB VI (Across DSB): 5′-GAGGAGCCTCTCCTGCAGC-3′, 5′-GAACCAGACCTACCTCCAGGG-3′.

Live cell imaging

U2OS cells stably expressing Rad52-mCherry, 53BP1-YFP, and Geminin-CFP constructs [21] were cultured on 35 mm glass bottom microwell dishes (MatTek, P35GC-1.5–10-C). Cells were treated with 0.5 μg/ml NCS to induce DSBs for 60 min at 37 °C. Subsequently, cells were washed twice with PBS before adding media containing DMSO or CK-666 (100 μM). For mirin experiments, cells were pre-treated with mirin (Sigma Aldrich: M9948, 50 μM) for 1 hour prior to addition of NCS, and subsequently washed and incubated with mirin for indicated time points. S-phase cells were selected for Rad52 foci analysis by screening for Geminin-CFP positivity. G1 cells were selected for 53BP1 foci analysis by screening for Geminin-CFP/Rad52-mCherry negative cells. After 20 hours, images were acquired on an A1RMP confocal microscope (Nikon Instruments, Melville, NY), on a TiE Eclipse stand equipped with a 60×/1.49 Apo-TIRF oil-immersion objective lens, an automated XY stage, stage-mounted piezoelectric focus drive, and a heated, humidified stagetop chamber with 5% CO_2 atmosphere. Cells expressing Rad52-mCherry and 53BP1-YFP foci were imaged in GaAsP detectors using 561 nm and 488 nm excitation, respectively, and standard RFP and GFP emission filters. The confocal pinhole was set to 1 Airy unit for the red channel. Foci movements were examined by collecting z series at 0.4 μm intervals throughout the entire nucleus every 5 min for 2.5 h. Focus was maintained by the Perfect Focus System (Nikon).

Nuclear actin-chromobody-tag-GFP imaging and analysis

For live cell imaging experiments, U2OS cells were cultured on 35 mm glass bottom microwell dishes at 90% confluency (MatTek, P35GC-1.5–10-C) and transfected with 0.3 μg of nuclear actin-chromobody-tag-GFP expressing vector (Chromotek, acg-n; EMD Millipore, FuGENE 6 transfection reagent; Promega) After six hours, cells were treated with 1 μg/ml NCS for 60 min at 37 °C. Cells were washed twice with PBS before adding media containing DMSO. After 3 hours, images were acquired on an A1RMP confocal microscope using equipment and settings described above. Cells with actin-cb foci were classified using the following criteria: actin-cb foci exhibited movement and frequent turnover, were round in morphology and often appeared to have fuzzy “tails”. Cells with actin-cb rods were classified using the following criteria: actin-cb rods exhibited limited movement, no turnover, were very bright, and were filamentous in morphology. Foci movements were examined by collecting z series at 0.4 μm intervals throughout the entire nucleus every 30 seconds for 10 min. Following initial image acquisition, cells were subsequently treated with

100 μM CK-666. Images of actin-cb foci were subsequently acquired 1 hour post CK-666 treatment. Actin-cb foci were scored as the number of discrete punctate structures appearing per nucleus, as detected by the Icy Spot Detector plug-in. For experiments assessing localization of actin cb foci with RPA, U2OS cells were co-transfected with actin-chromobody-tag-GFP and RPA32-NLS-mCherry (a kind gift of Jiri Lukas) for 16 hr prior to NCS treatment. After 12 hours, foci movements were examined by collecting z series at 0.4 μm intervals throughout the entire nucleus every 5 min for 2.5 h.

For experiments in fixed cells, U2OS cells were cultured on 8-well chamber slides (Thermo Fisher Scientific), subjected to transfection and drug treatments as described above, and processed for IHC as described above. Cells were stained with primary antibodies against Rad51 (Santa Cruz: sc-8349, 1/50) and GFP (Abcam: ab13970, 1/100) overnight. Secondary antibodies were Alexa 488 conjugated goat anti-chicken Ig (Invitrogen: A11039, 1/1000) and Alexa 594 conjugated goat anti-mouse Ig (Thermo Fisher Scientific, A-11005, 1/10000). Actin chromobody-expressing cells were selected for analysis by screening for actin-cb foci. Images were acquired on an A1RMP confocal microscope equipped with a 60×/1.49 Apo-TIRF oil-immersion objective lens. Z series at 0.4 μm intervals throughout the entire nucleus were acquired. For co-localization analysis, actin-cb and Rad51 foci were detected in Z using the spot detector plug-in available on Icy Bioimaging Software platform. The co-localization of Rad51 and actin-cb spots was assessed using the Co-localization Studio plug-in, object-based methodology. Here, co-localization was defined as the number of Rad51 spots that directly overlapped with or touched actin-cb foci (within a 0.7 μm radius).

DSB foci movement analysis

DSB movement analysis followed the approach recently described [9]. Nikon NIS Elements data files were processed in ImageJ [38]. Green and red channels were split and a maximum-intensity projection of each z stack was generated. T stacks were subsequently aligned using the StackReg plugin [25] to correct for cell movements over the duration of the experiment. Cells that underwent large-scale nuclear deformations or expansions were discarded. The TrackMate plug in for ImageJ [39] was used to perform single-particle tracking of DSB foci over a 100-min interval and monitor foci intensity. Foci trajectories were subsequently exported to Matlab and analyzed using the class @msdanalyzer [44]. The mean-square displacement (MSD) of DNA damage foci plots the average squared distance foci travel at increasing time intervals, whereas the diffusion coefficient *D(t)* is approximated through the linear-weighted fit of the initial mean MSD curve [40]. Mean-Square Displacement curves for DSB foci in a given cell were computed using the formula $MSD = \langle (x(t+\Delta t)-x(t))^2 \rangle$, where × reflects focus position and t is the time in minutes. For Rad52 foci, the weighted mean of all the MSD curves acquired from > 2000 tracks in 3 independent experiments is shown. The error bars for each point on the weighted mean of the MSD curve represent the weighted standard error of the mean over all MSD curves. The diffusion coefficient D(t) was estimated from the linear fit of the first 20% of each MSD curve. Calculation of the time-dependence coefficient α was determined using Matlab via log-log fitting of the power law $MSD(t) = \Gamma \times t^{\alpha}$. Cumulative distance (CD) traveled by foci over 100 min was calculated relative to their starting position using the formula: $D(i)=\mathrm{sqrt}(((X(i)-X(i-1))^2 + ((Y(i)-Y(i-1))^2)))$ where X and Y refer to the x and y coordinates of the focus at time i.

DSB foci clustering analysis

For analysis of DSB foci clustering during live cell imaging, a clustering event was defined as complete co-localization of ≥ 2 foci over ≥ 3 consecutive frames (15 min) over a 100 min interval. For actin-cb clustering during live cell imaging, a clustering event was defined as complete co-localization of ≥ 2 foci over ≥ 3 consecutive frames (3 min) over a 20 min interval.

Quantification of RPA association to chromatin by flow cytometry

Detection of chromatin-bound RPA in S-phase cells followed recently published protocols with the following modifications: 2×10^6 cells were treated with DMSO or 1 μg/ml camptothecin (CPT) for 24 hours. Cells were subsequently washed once with cold PBS, then incubated in cold CSK buffer + 1% Triton-X for 5 min. Cells were then washed with PBS and fixed in 0.5% PFA for 15 min. Cells were subsequently washed twice in BD Perm/Wash buffer (Becton-Dickinson: BD554723) and stained with RPA2/RPA32 antibody (Abcam: ab2175, 1:50) overnight. Cells were then washed with PBS and incubated in secondary antibody (Abcam: ab150113, 1/50 or Alexa 647 conjugated donkey anti-mouse Ig, Invitrogen: A31571, 1/50) for 1 h. Cells were then washed and stained with propidium iodide in the presence of RNAse A overnight. The percentage of S-phase cells as identified by PI staining was quantified by flow cytometry. The gate for RPA-positive cells was established using a negative control sample that was stained with mouse IgG following extraction. RPA-positive cells following DMSO and CPT treatment were subsequently quantified by flow cytometry. A minimum of 10000 cells were counted per biological replicate.

Clonogenic and cell survival assays

U2OS cells were seeded onto 10 cm dishes (1000 cells per dish) overnight. Cells were subsequently treated with 0, 100, 200, or 300 μM CK-666 in the presence of DMSO, camptothecin (CPT, 10 nM), or aphidocolin (APH, 400 nM) for 12 hours. Cells were then washed with PBS and incubated in fresh media 10–14 days. Cells were subsequently washed with PBS, fixed for 10 min with 100% methanol, and stained with 0.1% crystal violet for 10 min. For olaparib studies, cells were treated with 0, 10, or 20 μM CK-666 in the presence of DMSO or 50 nM Olaparib for 14 days, and fixed and stained was above. Each experiment was performed in triplicate.

For colony quantification, images of dishes were converted to Grayscale and processed with Icy Software (Version 1.8.6.0; Institut Pasteur, Quantitative Image Analysis Unit; http://www.icy.bioimageanalysis.org). Regions of interest were drawn around individual dishes and colonies were counted using the Spot Detector plug-in (Channel 0). Counts from two biological replicates were normalized for plating efficiency.

For Annexin V/propidium iodide survival assay, $1–5 \times 10^5$ cells were incubated in DMSO or 1 μg/ml CPT for 0, 12, or 24 hours. Cells were then washed in 1X binding buffer (Thermo Fisher Scientific: 00-0055) and stained with APC-conjugated Annexin V (Thermo Fisher Scientific: 17-8007) for 10 min. Cells were then washed in 1X binding buffer and stained in propidium iodide (Thermo Fisher Scientific: 00-6990). Percent viability following CPT

treatment was assessed by measuring the percentage of APC-Annexin V-negative and propidium iodide-negative cells by flow cytometry. A minimum of 10,000 cells counted per condition.

Quantification and Statistical Analysis

Statistical parameters are reported in the Figures and the Figure Legends. Two-tailed t-tests and Ordinary one-way ANOVAs were used for comparisons of means of normally distributed data and two-tailed Mann-Whitney U tests were used for comparison of non-normally distributed data. Statistical analyses were performed using Prism 7.0.

Research Animals

The use of *Xenopus laevis* (African clawed frog) in this research proposal is approved (protocol AAAK0551) by the Institutional Animal Care and Use Committee (IACUC) of Columbia University Medical School. All procedures comply with Public Health Service's policies for the humane care and use of laboratory animals.

Data Availability

The data that support the findings of this study are available from the corresponding author upon reasonable request. The authors declare that the data supporting the findings of this study are available within the paper [and its Supplementary Information files].

Extended Data

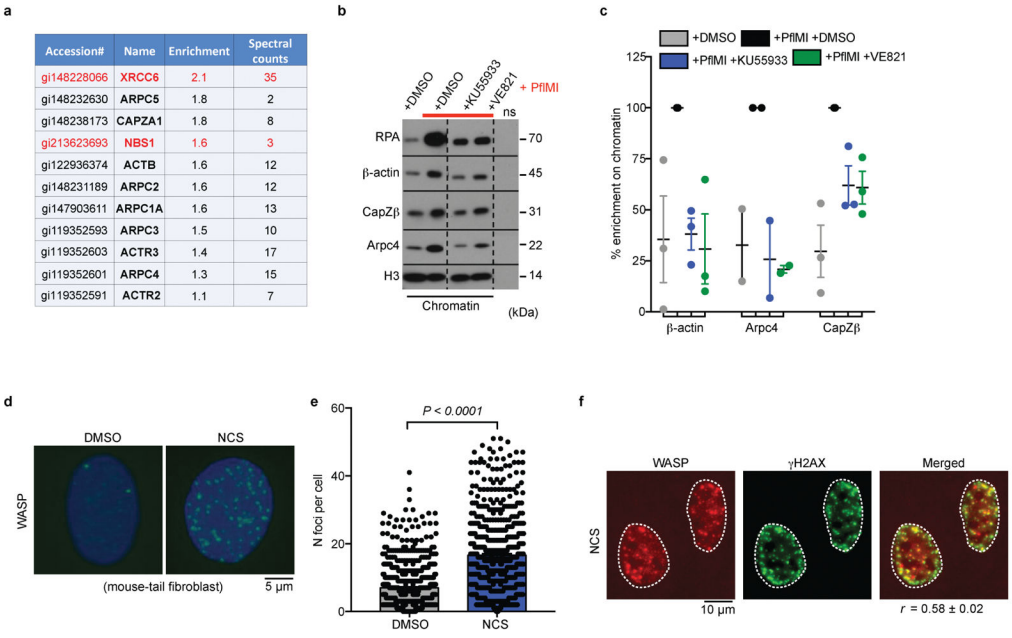

Accession#	Name	Enrichment	Spectral counts
gi148228066	XRCC6	2.1	35
gi148232630	ARPC5	1.8	2
gi148238173	CAPZA1	1.8	8
gi213623693	NBS1	1.6	3
gi122936374	ACTB	1.6	12
gi148231189	ARPC2	1.6	12
gi147903611	ARPC1A	1.6	13
gi119352593	ARPC3	1.5	10
gi119352603	ACTR3	1.4	17
gi119352601	ARPC4	1.3	15
gi119352591	ACTR2	1.1	7

Extended Data Fig. 1. Actin filament nucleators localize to chromosomal DSBs in *Xenopus* extracts and mammalian cells

a, Enrichment ratios and spectral counts of actin complexes and repair proteins in DSB-containing chromatin by liquid chromatography-mass spectrometry are shown. **b,** DNA damage-dependent enrichment of actin complexes (+PflMI) following PIKK inhibition

(KU55933: ATMi; VE821: ATRi). RPA shown as a marker of DNA damage. **c,** Quantification actin complexes in chromatin relative to + PflMI samples. (β-actin n=3 independent experiments, Arpc4 n=2 independent experiments, CapZβ n=3 independent experiments). Mean and s.e.m shown. **d,** Representative images of WASP foci post NCS treatment in MTFs. **e,** Quantification of WASP foci (*P* calculated by two-sided Mann-Whitney test; data shown as mean; DMSO n=578 nuclei, NCS n=556 nuclei). **f,** γH2AX co-localization with WASP foci in MTFs (n = 22 nuclei, r = 0.58 ± 0.021, Pearson). Scale bar is 5 μm or as shown.

a

	Treatment	No cells analyzed (No foci)	Cumulative Distance ± SD (μm)	Diffusion coefficient (10^{-5} μm^2/s)	Anomalous Diffusion Coefficient ± SE	No of experiments
Rad52-mCherry, U2OS (100 min)	DMSO	12 (3292)	4.2 ± 1.29	4.38	0.719 ± 0.006	3
	CK-689 (100 μM)	13 (3262)	3.8 ± 1.08	3.65	0.726 ± 0.006	3
	CK-666 (100 μM)	12 (2143)	3.2 ± 1.05	1.96	0.589 ± 0.009	3
	Mirin (50 μM)	11 (2677)	3.3 ± 0.92	2.36	0.643 ± 0.007	2
53BP1-YFP, U2OS (G1) (100 min)	DMSO	12 (893)	3.6 ± 1.03	2.93	0.715 ± 0.011	2
	CK-689 (100 μM)	14 (926)	3.3 ± 0.89	2.41	0.709 ± 0.012	2
	CK-666 (100 μM)	14 (1234)	3.2 ± 1.03	2.32	0.669 ± 0.009	2
	Mirin (50 μM)	14 (774)	3.3 ± 1.05	2.35	0.685 ± 0.013	2
RPA32-pEGFP-NLS, MTF (100 min)	DMSO	10 (1031)	3.7 ± 1.03	3.27	0.731 ± 0.013	2
	CK-689 (100 μM)	13 (790)	4.0 ± 1.25	4.08	0.743 ± 0.012	2
	CK-666 (100 μM)	12 (823)	3.4 ± 1.01	2.07	0.66 ± 0.013	2
	Arpc2 -/- (4μM 4-OHT)	13 (1135)	3.2 ± 1.09	1.76	0.60 ± 0.011	2

b

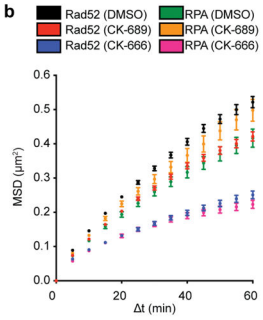

Extended Data Fig. 2. CK-689 does not significantly impact foci movement

a, Summary of DSB movement analyses as related to Figures 3, 6, and Extended Data Figure 5. **b,** MSD of Rad52-mCherry foci and RPA-pEGFP-NLS foci treated with DMSO, CK-689 and CK-666. (Data shown as mean and weighted s.e.m.; Rad52: CK-689 n=3262 foci from 13 nuclei, CK-666 n=2143 foci from 12 nuclei, DMSO n=3292 foci from 12 nuclei. RPA32: CK-689 n=790 foci from 13 nuclei, CK-666 n=823 foci from 12 nuclei, DMSO n=1031 foci from 10 nuclei). MSD of Rad52 DMSO also shown in Fig. 6i. MSD of Rad52 CK-689 and CK-666 also shown in Fig. 3g. MSD of RPA CK-689 and CK-666 also shown in Fig. 3l.

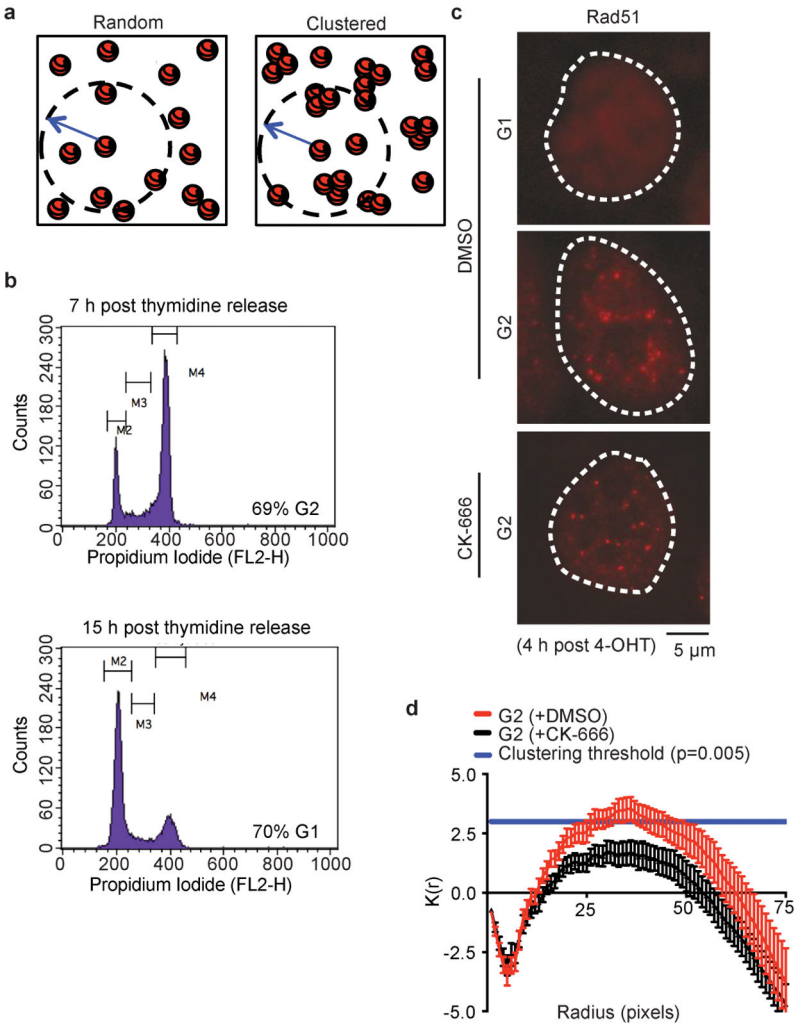

Extended Data Fig. 3. Arp2/3 clusters Rad51 foci

a, Schematic of clustering events. **b,** Representative cell cycle distribution of U2OS cells following double-thymidine block (out of five independent experiments). **c,** Representative images of U2OS-AsiSI nuclei showing Rad51 foci. **d,** Rad51 foci clustering in G2 cells (*P* calculated by Spatial analysis plug-in; data shown as mean and s.e.m. of Ripley function; DMSO n=95 nuclei, CK-666 n=80 nuclei).

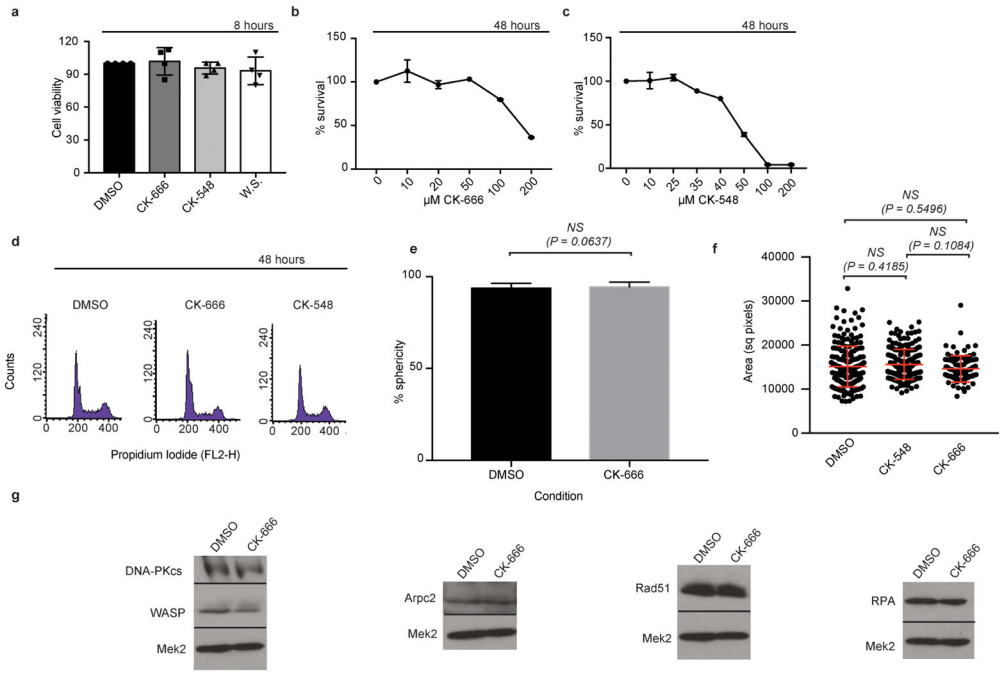

Extended Data Fig. 4. WASP and Arp2/3 inactivation do not impair U2OS cell viability, nuclear area, nuclear sphericity or protein expression

a, Cell survival after 8 hours of 100 µM CK-666, 50 µM CK-548, or 3 µM Wiskostatin treatment. Data shown as mean and s.e.m. n=4 independent experiments. **b,** Cell survival after 48 hours of increasing concentrations of CK-666. n=3 independent experiments. Data shown as mean and s.e.m. **c,** Cell survival after 48 hours of increasing concentrations of CK-548. n=3 independent experiments. Data shown as mean and s.e.m. **d,** Representative cell-cycle distribution of cells treated with DMSO, 50 µM CK-666, or 25 µM CK-548 for 48 hours (out of three independent experiments). **e,** Analysis of nuclear sphericity (*P* calculated by Student's two-tailed t-test; data shown as mean and s.d.; DMSO n=117 nuclei, CK-666 n=117 nuclei). ns, not significant. **f,** Analysis of nuclear area (*P* calculated by one-way ANOVA with multiple comparisons; data shown as mean and s.d.; DMSO n=210 nuclei, CK-548 n=189 nuclei, CK-666 n=92 nuclei). **g,** Expression of Rad51, DNA-PK(cs), WASP, and Arpc2 validating antibodies employed in Fig. 2e–i (single experiment). Mek2 is a loading control. RPA expression levels also shown.

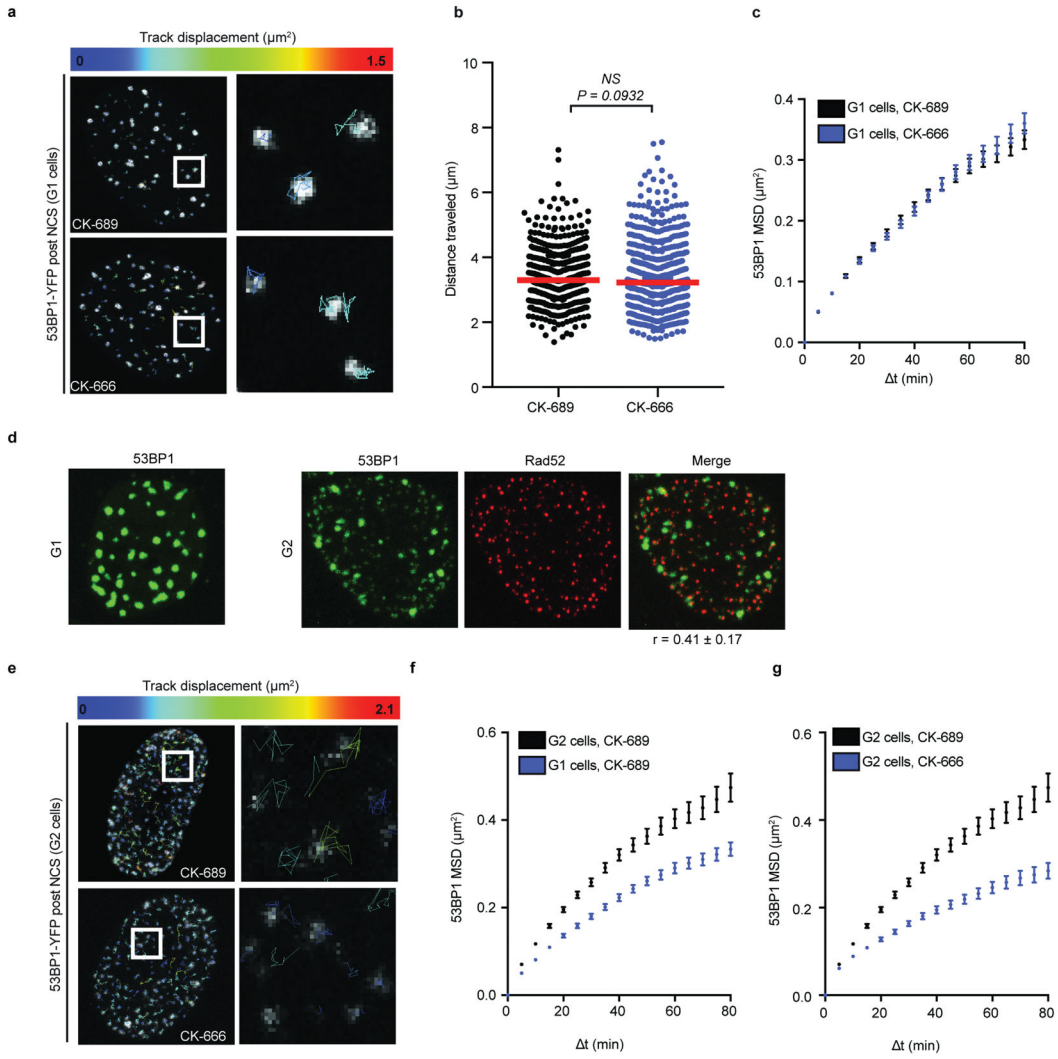

Extended Data Fig. 5. Arp2/3 enhances movement of 53BP1 foci in G2

a, Representative U2OS nuclei showing 53BP1-YFP foci traces over 100 min in G1 cells **b,** Median cumulative distance traveled by 53BP1-YFP foci in G1 cells (*P* calculated by two-tailed Mann-Whitney test; CK-689 n=462 foci from 14 nuclei, CK-666 n=647 foci from 14 nuclei). ns, not significant. **c,** MSD of 53BP1-YFP foci in G1 cells (Data shown as mean and weighted s.e.m.; CK-689 n=926 foci from 14 nuclei, CK-666 n=1234 foci from 14 nuclei). Δt = time interval. **d,** A representative G1 cell is shown with 53BP1-YFP foci (left). A representative G2 cell is shown with 53BP1-YFP and Rad52-mCherry foci (right). 53BP1 foci colocalize with Rad52 foci (r = 0.41 ± 0.17, Pearson, n=5 independent experiments). **e,** Representative U2OS nuclei showing 53BP1-YFP foci traces over 100 min in G2 cells. **f,** MSD of 53BP1-YFP foci (Data shown as mean and weighted s.e.m.; G1 CK-689 n=926 foci from 14 nuclei, G2 CK-689 n=1403 from 12 nuclei). G1 CK-689 curve also shown in (c). **g,** MSD of 53BP1-YFP foci in G2 cells (Data shown as mean and weighted s.e.m.; CK-689 n=1403 foci from 12 nuclei, CK-666 n=1038 foci from 10 nuclei). G2 CK-689 curve also shown in (f).

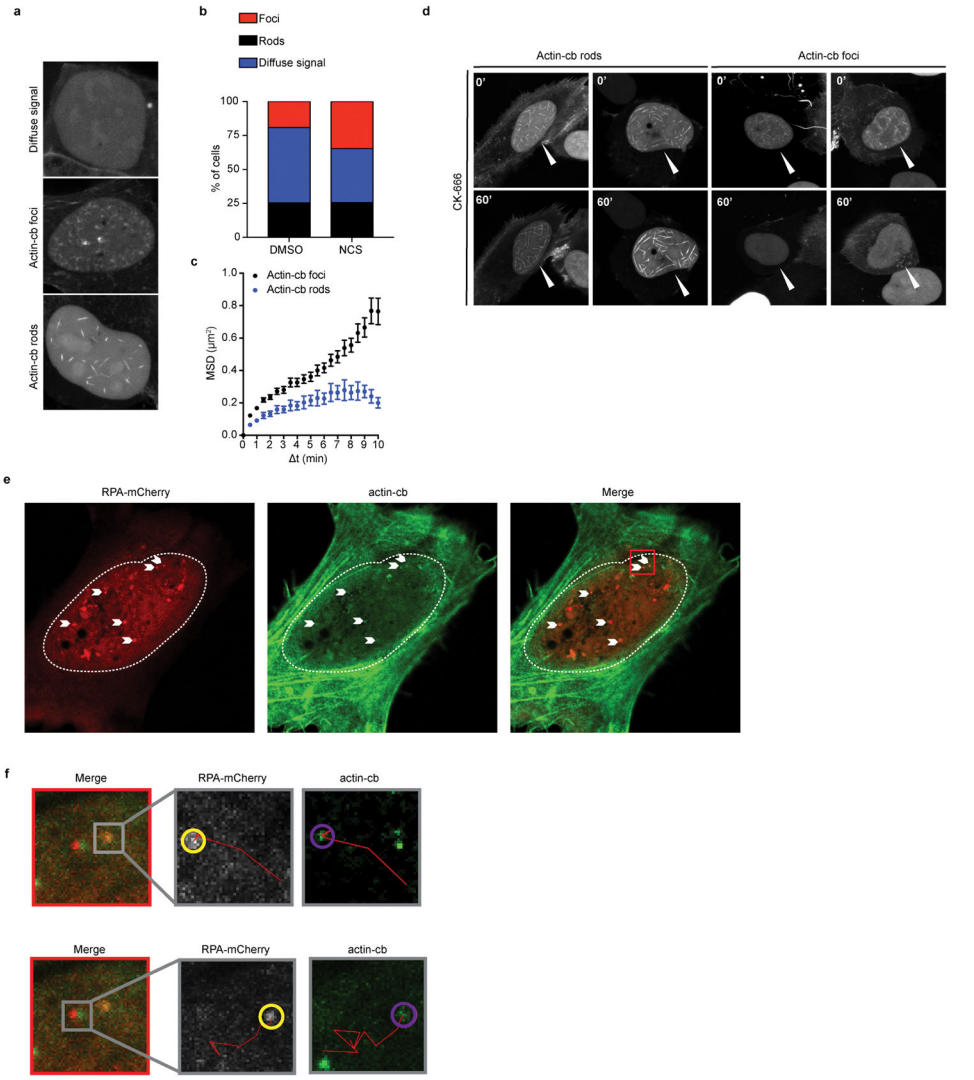

Extended Data Fig. 6. Arp2/3 promotes actin foci assembly following DNA damage

a, Representative U2OS nuclei showing classes of nuclear actin structures following transient transfection of nuclear actin-chromobody-tag-GFP. **b,** Percentage of cells with diffuse signal, nuclear actin-cb foci, or rods with or without NCS (DMSO n=473 cells, NCS n=473 cells). **c,** MSD of actin-cb foci and actin-cb rods (Data shown as mean and weighted s.e.m.; actin-cb foci n=662 foci from 11 nuclei, actin-cb rods n=161 rods from 5 nuclei). **d,** Representative images of U2OS nuclei with actin rods or actin-cb foci following CK-666 treatment (n=5 independent experiments). **e,** Representative image of a U2OS nucleus with RPA-mCherry and actin-cb foci (of n=3 independent experiments). Arrowheads indicate sites of RPA-mCherry and actin-cb co-localization. **f,** Expanded image of RPA-mCherry and actin-cb co-localization from **e,** red box. Traces of RPA and actin-cb foci are shown in red. Yellow and purple circles encompass RPA and actin-cb foci, respectively. (n=3 independent experiments).

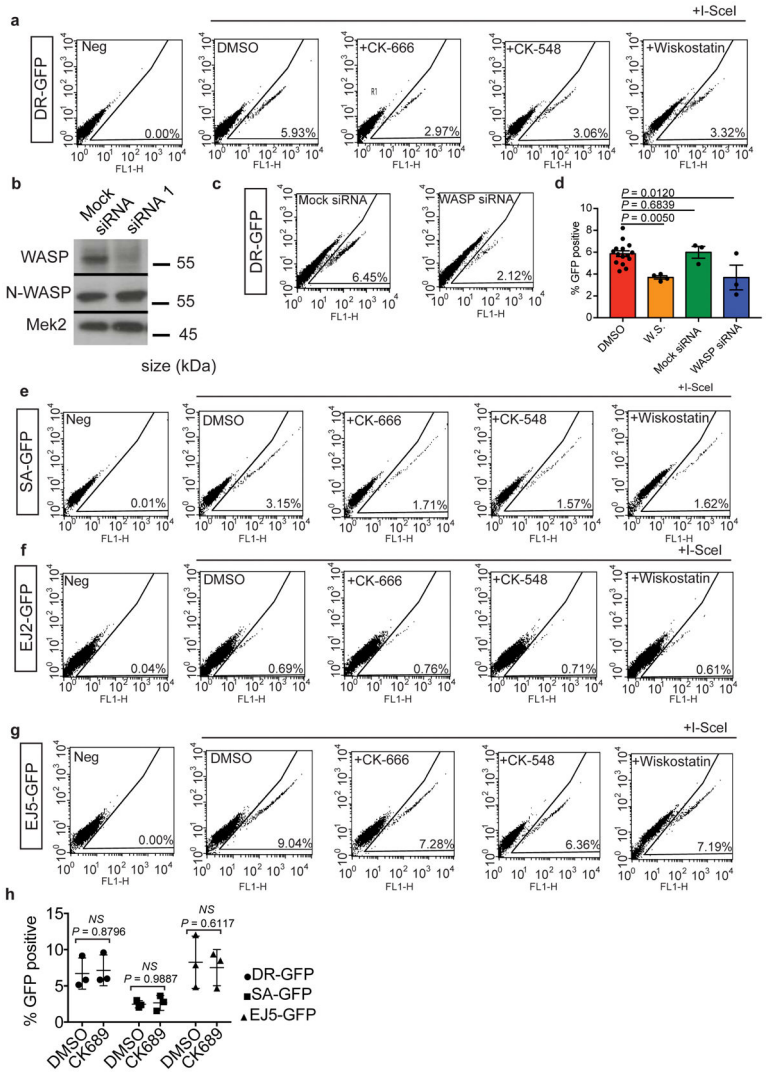

Extended Data Fig. 7. WASP and Arp2/3 mediate DSB repair by homology-directed mechanisms

a, Representative FACS plots of GFP$^+$ cells in the HDR (DR-GFP) assay. **b,** Western blot shows expression of WASP and N-WASP following siRNA knockdown in whole cell lysates (single experiment). WASP siRNA 1: 5′-GAGUGGCUGAGUUACUUGC-3′. **c,** Representative FACS plots of GFP$^+$ cells in the HDR (DR-GFP) assay in WASP and mock-depleted cells. **d,** Summary of DR-GFP assay with WASP depletion (*P* calculated by one-way ANOVA with multiple comparisons; data shown as mean and s.e.m; n=3 independent experiments). HDR efficiency in the presence of DMSO or Wiskostatin (Fig. 5a) shown for comparison. **e,** Representative FACS plots of GFP$^+$ cells in the SSA (SA-GFP) assay. **f,** Representative FACS plots of GFP$^+$ cells in the MMEJ (EJ2-GFP) assay. **g,** Representative FACS plots of GFP$^+$ cells in the NHEJ (EJ5-GFP) assay. **h,** Summary of DR-GFP, SA-GFP, and EJ5-GFP assays with CK-689 (*P* calculated by two-way ANOVA with multiple comparisons; data shown as mean and s.d.; n=3 independent experiments). n.s = not significant.

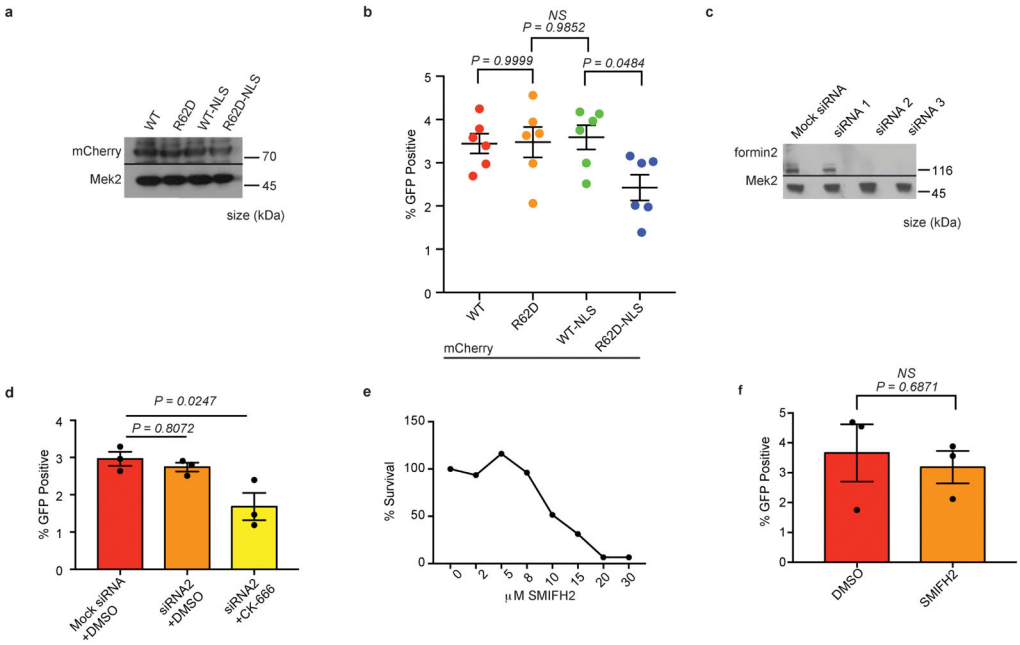

Extended Data Fig. 8. Actin nucleation regulates HDR in the nucleus and does not require formin-2 activity

a, Western blot shows expression of mCherry-tagged actin constructs in U2OS whole cell lysates (single experiment). **b,** Summary of DR-GFP (HDR) assay (*P* calculated by one-way ANOVA with multiple comparisons; data shown as mean and s.e.m; n=6 independent experiments). **c,** Western blot shows knockdown of formin-2 following 48 hr transfection of mock or sequence-specific siRNA oligos (single experiment). Formin-2 siRNA #2: 5′-CGUGUAAUCAGAAUGCCCA-3′. **d,** Summary of DR-GFP assay (*P* calculated by one-way ANOVA with multiple comparisons; data shown as mean and s.e.m; n=3 independent experiments). **e,** Mean cell survival after 48 hours of increasing concentrations of the formin inhibitor, SMIFH2 (n=3 independent experiments). **f,** Summary of DR-GFP assay (*P* calculated by student's two-tailed t-test; data shown as mean and s.e.m; n=3 independent experiments).

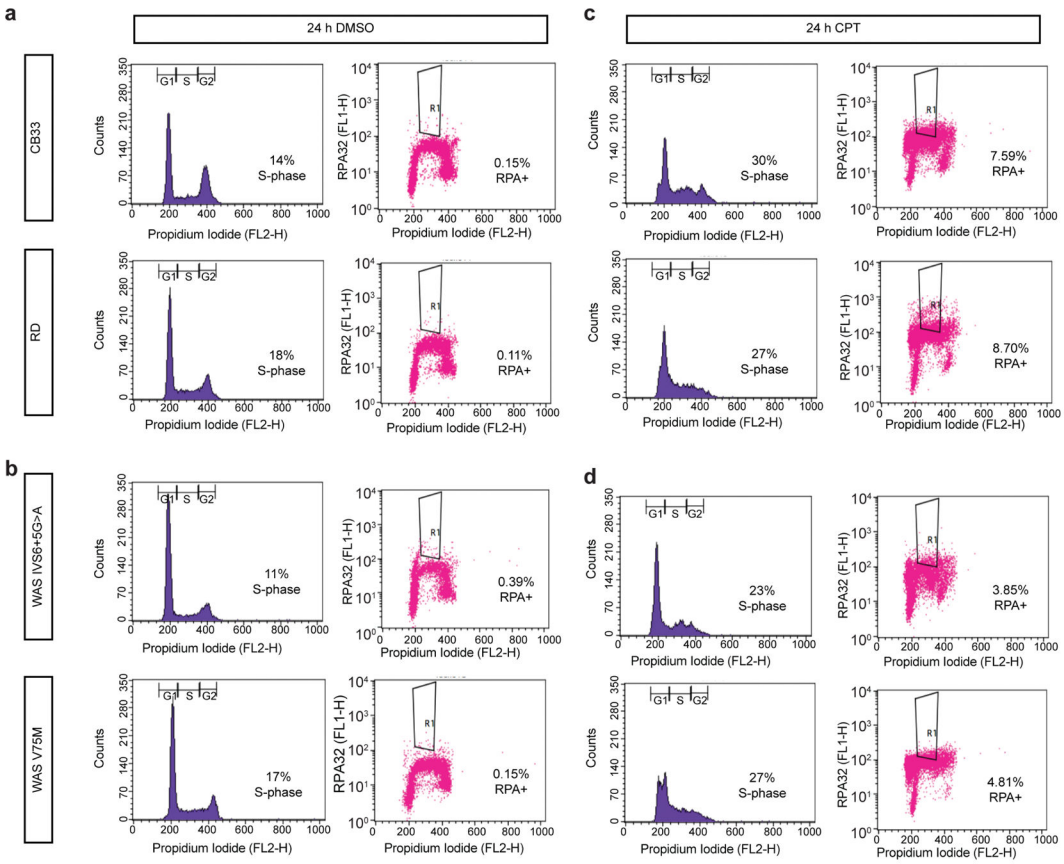

Extended Data Fig. 9. B-lymphocytes derived from Wiskott-Aldrich Syndrome patients exhibit reduced DSB end-resection

a, Representative cell cycle distribution of CB33 and RD lymphocytes derived from healthy controls following DMSO treatment is shown (left). The percentage RPA positive S-phase cells following DMSO treatment was measured by flow cytometry (right). (n=4 independent experiments). **b,** Representative cell cycle distribution of lymphocytes bearing the V75M mutation in the WAS gene or a G>A transition at position 5 in intron 6 of the WAS gene (IVS6+5G>A) is shown following DMSO treatment (left). The percentage RPA positive S-phase cells following DMSO treatment was measured by flow cytometry (right). (n=4 independent experiments). **c,** Representative cell cycle distribution of CB33 and RD lymphocytes derived from healthy controls following CPT treatment (left). The percentage RPA positive S-phase cells following CPT treatment was measured by flow cytometry (right). (n=4 independent experiments). **d,** The cell cycle distribution of V75M or IVS6+5G>A lymphocytes following CPT treatment is shown (left). The percentage RPA positive S-phase cells following CPT treatment was measured by flow cytometry (right). (n=4 independent experiments).

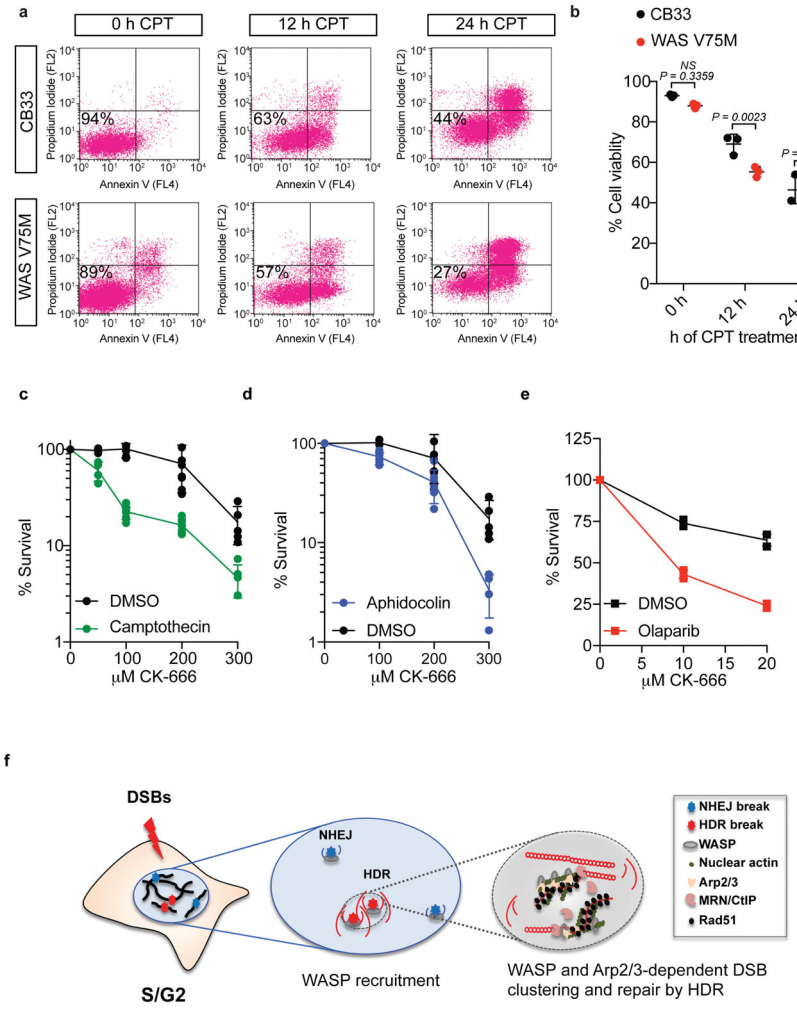

Extended Data Fig. 10. Arp2/3 inactivation confers sensitivity to DSBs induced in S-phase as well as replication stress-inducing agents

a, Control CB33 lymphocytes or lymphocytes bearing a V75M mutation in the WAS gene were treated with camptothecin (CPT) for 0, 12, or 24 hours. Percent viability following CPT treatment was assessed by measuring the fraction of Annexin V and propidium iodide negative cells by flow cytometry. **b,** Summary of CB33 or WAS V75M lymphocyte survival following CPT treatment (*P* calculated by two-way ANOVA with multiple comparisons; data shown as mean and s.d.; n=3 independent experiments) **c,** Clonogenic U2OS cell survival after 12 hr of camptothecin treatment in the presence of DMSO or increasing concentrations of CK-666. (Triplicate experiments; data shown as mean and s.d.; n=2 independent experiments). **d,** Clonogenic U2OS cell survival after 12 hr of aphidicolin treatment in the presence of DMSO or increasing concentrations of CK-666. (Triplicate experiments; data shown as mean and s.d.; n=2 independent experiments). **e,** Clonogenic U2OS cell survival after olaparib treatment in the presence of DMSO or increasing concentrations of CK-666 for 14 days. (Triplicate experiments; data shown as mean and s.e.m.; n=2 independent experiments). **f,** DNA damage induces DSBs, which are repaired preferentially by NHEJ in mammalian cells (in blue). In S/G2, DSBs may be repaired by HDR (in red). All DSBs recruit WASP, but Arp2/3-dependent actin polymerization occurs only at HDR breaks,

which become more mobile. Actin polymerization in the vicinity of DSBs generates forces resulting in DSB clustering, optimal DNA end resection, Rad51 foci formation, and HDR.

Supplementary Material

Refer to Web version on PubMed Central for supplementary material.

Acknowledgments

We thank T. Swayne and E.L. Munteanu from the Confocal and Specialized Microscopy Shared Resource of the Irving Cancer Research Center (ICRC) and the Flow Cytometry Shared Resource of the ICRC at Columbia University (supported by NIH grants #P30-CA013696, #S10-RR025686). We also thank J. Stark for the GFP reporter cell lines; G. Legube for the ER-AsiSI U2OS lines and for sharing unpublished data; J. Bear for the Arpc2-LoxP-CreER MTFs; G. Lahav for the Rad52-mCherry U2OS line; J. Lukas for the pEGFP-NLS-RPA32 construct; R. Baer for the I-SceI plasmid; N. Kato and T. Lagache for manuscript comments; and A. Hollar for Metacyte classifier design. This work was supported by the NIH (R35-CA197606 and P01-CA174653 to J.G., RO1-GM099481 to G.G.G., PHS-GM103314 and PHS-GM109824 to B.T.C., and F30-CA217049 to B.R.S.)

References

1. Dion V, Kalck V, Horigome C, Towbin BD, Gasser SM. Increased mobility of double-strand breaks requires Mec1, Rad9 and the homologous recombination machinery. Nat Cell Biol. 2012; 14:502–509. DOI: 10.1038/ncb2465 [PubMed: 22484486]
2. Mine-Hattab J, Rothstein R. Increased chromosome mobility facilitates homology search during recombination. Nat Cell Biol. 2012; 14:510–517. DOI: 10.1038/ncb2472 [PubMed: 22484485]
3. Lisby M, Mortensen UH, Rothstein R. Colocalization of multiple DNA double-strand breaks at a single Rad52 repair centre. Nat Cell Biol. 2003; 5:572–577. DOI: 10.1038/ncb997 [PubMed: 12766777]
4. Aten JA, et al. Dynamics of DNA double-strand breaks revealed by clustering of damaged chromosome domains. Science. 2004; 303:92–95. DOI: 10.1126/science.1088845 [PubMed: 14704429]
5. Aymard F, et al. Genome-wide mapping of long-range contacts unveils clustering of DNA double-strand breaks at damaged active genes. Nat Struct Mol Biol. 2017; 24:353–361. DOI: 10.1038/nsmb.3387 [PubMed: 28263325]
6. Lemaitre C, et al. Nuclear position dictates DNA repair pathway choice. Genes Dev. 2014; 28:2450–2463. DOI: 10.1101/gad.248369.114 [PubMed: 25366693]
7. Robinett CC, et al. In vivo localization of DNA sequences and visualization of large-scale chromatin organization using lac operator/repressor recognition. J Cell Biol. 1996; 135:1685–1700. [PubMed: 8991083]
8. Soutoglou E, et al. Positional stability of single double-strand breaks in mammalian cells. Nat Cell Biol. 2007; 9:675–682. DOI: 10.1038/ncb1591 [PubMed: 17486118]
9. Cho NW, Dilley RL, Lampson MA, Greenberg RA. Interchromosomal homology searches drive directional ALT telomere movement and synapsis. Cell. 2014; 159:108–121. DOI: 10.1016/j.cell.2014.08.030 [PubMed: 25259924]
10. Lottersberger F, Karssemeijer RA, Dimitrova N, de Lange T. 53BP1 and the LINC Complex Promote Microtubule-Dependent DSB Mobility and DNA Repair. Cell. 2015; 163:880–893. DOI: 10.1016/j.cell.2015.09.057 [PubMed: 26544937]
11. Virtanen JA, Vartiainen MK. Diverse functions for different forms of nuclear actin. Curr Opin Cell Biol. 2017; 46:33–38. DOI: 10.1016/j.ceb.2016.12.004 [PubMed: 28092729]
12. Taylor MD, et al. Nuclear role of WASp in the pathogenesis of dysregulated TH1 immunity in human Wiskott-Aldrich syndrome. Sci Transl Med. 2010; 2:37ra44.
13. Wu X, et al. Regulation of RNA-polymerase-II-dependent transcription by N-WASP and its nuclear-binding partners. Nat Cell Biol. 2006; 8:756–763. DOI: 10.1038/ncb1433 [PubMed: 16767080]

14. Yoo Y, Wu X, Guan JL. A novel role of the actin-nucleating Arp2/3 complex in the regulation of RNA polymerase II-dependent transcription. J Biol Chem. 2007; 282:7616–7623. DOI: 10.1074/jbc.M607596200 [PubMed: 17220302]
15. Pollard TD, Borisy GG. Cellular motility driven by assembly and disassembly of actin filaments. Cell. 2003; 112:453–465. [PubMed: 12600310]
16. Belin BJ, Lee T, Mullins RD. DNA damage induces nuclear actin filament assembly by Formin -2, Spire-(1/2) that promotes efficient DNA repair [corrected]. Elife. 2015; 4:e07735. [PubMed: 26287480]
17. Hetrick B, Han MS, Helgeson LA, Nolen BJ. Small molecules CK-666 and CK-869 inhibit actin-related protein 2/3 complex by blocking an activating conformational change. Chem Biol. 2013; 20:701–712. DOI: 10.1016/j.chembiol.2013.03.019 [PubMed: 23623350]
18. Nolen BJ, et al. Characterization of two classes of small molecule inhibitors of Arp2/3 complex. Nature. 2009; 460:1031–1034. DOI: 10.1038/nature08231 [PubMed: 19648907]
19. Rogakou EP, Boon C, Redon C, Bonner WM. Megabase chromatin domains involved in DNA double-strand breaks in vivo. J Cell Biol. 1999; 146:905–916. [PubMed: 10477747]
20. Aymard F, et al. Transcriptionally active chromatin recruits homologous recombination at DNA double-strand breaks. Nat Struct Mol Biol. 2014; 21:366–374. DOI: 10.1038/nsmb.2796 [PubMed: 24658350]
21. Karanam K, Kafri R, Loewer A, Lahav G. Quantitative live cell imaging reveals a gradual shift between DNA repair mechanisms and a maximal use of HR in mid S phase. Mol Cell. 2012; 47:320–329. DOI: 10.1016/j.molcel.2012.05.052 [PubMed: 22841003]
22. Ochs F, et al. 53BP1 fosters fidelity of homology-directed DNA repair. Nat Struct Mol Biol. 2016; 23:714–721. DOI: 10.1038/nsmb.3251 [PubMed: 27348077]
23. Rotty JD, et al. Profilin-1 serves as a gatekeeper for actin assembly by Arp2/3-dependent and -independent pathways. Dev Cell. 2015; 32:54–67. DOI: 10.1016/j.devcel.2014.10.026 [PubMed: 25543281]
24. Caron P, et al. Non-redundant Functions of ATM and DNA-PKcs in Response to DNA Double-Strand Breaks. Cell Rep. 2015; 13:1598–1609. DOI: 10.1016/j.celrep.2015.10.024 [PubMed: 26586426]
25. Plessner M, Melak M, Chinchilla P, Baarlink C, Grosse R. Nuclear F-actin formation and reorganization upon cell spreading. J Biol Chem. 2015; 290:11209–11216. DOI: 10.1074/jbc.M114.627166 [PubMed: 25759381]
26. Gunn A, Stark JM. I-SceI-based assays to examine distinct repair outcomes of mammalian chromosomal double strand breaks. Methods Mol Biol. 2012; 920:379–391. DOI: 10.1007/978-1-61779-998-3_27 [PubMed: 22941618]
27. Peterson JR, et al. Chemical inhibition of N-WASP by stabilization of a native autoinhibited conformation. Nat Struct Mol Biol. 2004; 11:747–755. DOI: 10.1038/nsmb796 [PubMed: 15235593]
28. Symington LS, Gautier J. Double-strand break end resection and repair pathway choice. Annu Rev Genet. 2011; 45:247–271. DOI: 10.1146/annurev-genet-110410-132435 [PubMed: 21910633]
29. Dupre A, et al. A forward chemical genetic screen reveals an inhibitor of the Mre11-Rad50-Nbs1 complex. Nat Chem Biol. 2008; 4:119–125. DOI: 10.1038/nchembio.63 [PubMed: 18176557]
30. Massaad MJ, Ramesh N, Geha RS. Wiskott-Aldrich syndrome: a comprehensive review. Ann N Y Acad Sci. 2013; 1285:26–43. DOI: 10.1111/nyas.12049 [PubMed: 23527602]
31. Tsouroula K, et al. Temporal and Spatial Uncoupling of DNA Double Strand Break Repair Pathways within Mammalian Heterochromatin. Mol Cell. 2016; 63:293–305. DOI: 10.1016/j.molcel.2016.06.002 [PubMed: 27397684]
32. Chiolo I, et al. Double-strand breaks in heterochromatin move outside of a dynamic HP1a domain to complete recombinational repair. Cell. 2011; 144:732–744. DOI: 10.1016/j.cell.2011.02.012 [PubMed: 21353298]
33. van Pel DM, Stirling PC, Minaker SW, Sipahimalani P, Hieter P. Saccharomyces cerevisiae genetics predicts candidate therapeutic genetic interactions at the mammalian replication fork. G3 (Bethesda). 2013; 3:273–282. DOI: 10.1534/g3.112.004754 [PubMed: 23390603]

34. Peterson SE, et al. Cdk1 uncouples CtIP-dependent resection and Rad51 filament formation during M-phase double-strand break repair. J Cell Biol. 2011; 194:705–720. DOI: 10.1083/jcb.201103103 [PubMed: 21893598]

35. Rappsilber J, Ishihama Y, Mann M. Stop and go extraction tips for matrix-assisted laser desorption/ionization, nanoelectrospray, and LC/MS sample pretreatment in proteomics. Anal Chem. 2003; 75:663–670. [PubMed: 12585499]

36. Lagache T, Lang G, Sauvonnet N, Olivo-Marin JC. Analysis of the spatial organization of molecules with robust statistics. PLoS One. 2013; 8:e80914. [PubMed: 24349021]

37. Zhou Y, Caron P, Legube G, Paull TT. Quantitation of DNA double-strand break resection intermediates in human cells. Nucleic Acids Res. 2014; 42:e19. [PubMed: 24362840]

38. Schindelin J, et al. Fiji: an open-source platform for biological-image analysis. Nat Methods. 2012; 9:676–682. DOI: 10.1038/nmeth.2019 [PubMed: 22743772]

39. Tinevez JY, et al. TrackMate: An open and extensible platform for single-particle tracking. Methods. 2017; 115:80–90. DOI: 10.1016/j.ymeth.2016.09.016 [PubMed: 27713081]

40. Tarantino N, et al. TNF and IL-1 exhibit distinct ubiquitin requirements for inducing NEMO-IKK supramolecular structures. J Cell Biol. 2014; 204:231–245. DOI: 10.1083/jcb.201307172 [PubMed: 24446482]

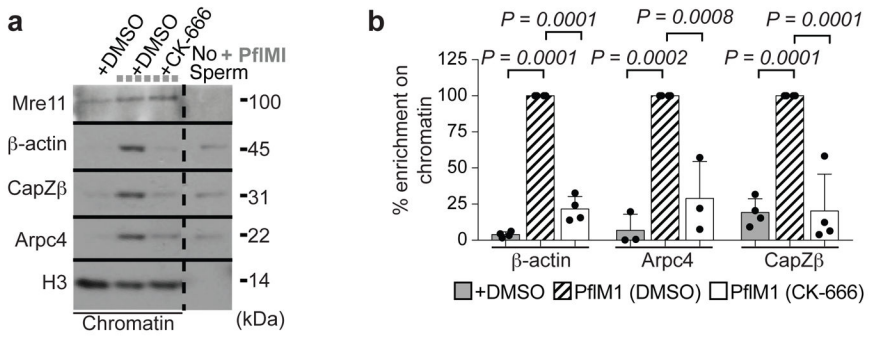

Figure 1. Actin complexes are recruited to damaged chromatin

a, Enrichment of actin complexes in damaged chromatin (+PflMI) by Western blot. Mre11 indicates DNA damage. **b,** Protein quantification in chromatin relative to +PflMI samples. (*P* calculated by one-way ANOVA with multiple comparisons; data shown as mean and s.d.; n=5, 3, and 4 independent experiments, left to right).

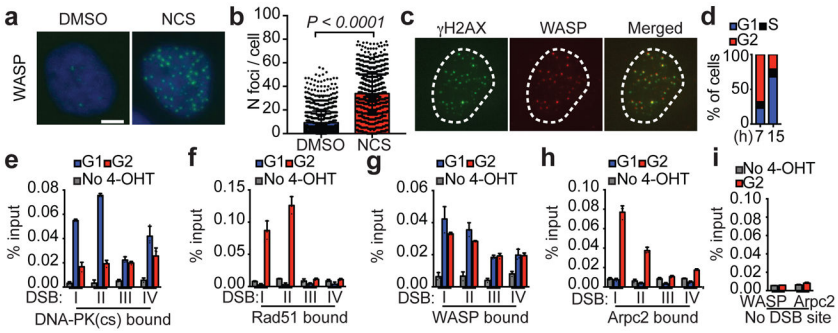

Figure 2. Arp2/3 and WASP co-localize at HDR breaks

a, Representative U2OS cells with WASP foci. **b,** Quantification of WASP foci (*P* calculated by two-sided Mann-Whitney test; data shown as mean and s.d.; n=1231 (DMSO), 1327 nuclei (NCS). **c,** γH2AX co-localization with WASP (n=30 nuclei; *r*=0.60±0.07, Pearson). **d,** Cell cycle distribution of synchronized ER-AsiSI-U2OS cells post thymidine release. DNA-PKcs (**e,**) Rad51 (**f,**) WASP (**g,**) and Arpc2 (**h,**) enrichment (ChIP) at DSBs I–IV in G1 and G2. Mean and s.d. (n=3 technical replicates) of a representative experiment (out of two independent experiments). **i,** Mean and s.d. of Arpc2 and WASP enrichment at an undamaged site in G2 cells (n=3 technical replicates) of a representative experiment (out of two independent experiments). Scale bar is 10 μm.

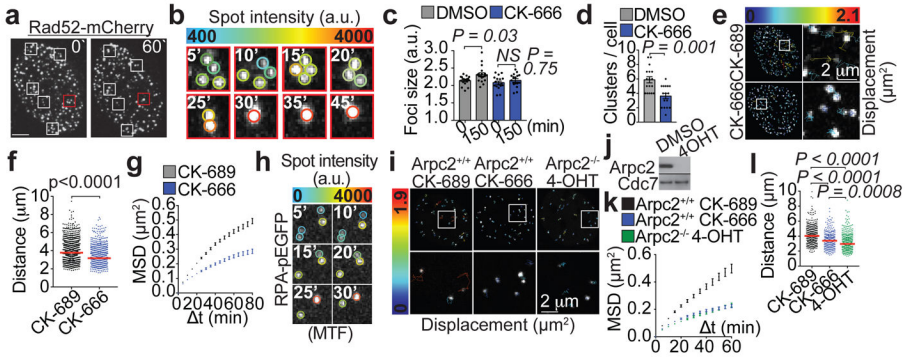

Figure 3. Arp2/3 drives DSB mobility during HDR

a, A representative U2OS nucleus with boxes indicating Rad52-mCherry foci clustering events. **b,** Expanded images of clustering from **a,** red box. Circles denote foci intensity. **c,** Rad52 foci size (*P* calculated by one-way ANOVA with multiple comparisons; data shown as mean and s.e.m.; n=19 (DMSO), 17 nuclei (CK-666). **d,** Rad52-mCherry clustering events (*P* calculated by two-tailed Mann-Whitney test; data shown as mean and s.e.m.; n=17 (DMSO), 16 nuclei (CK-666). **e,** Rad52-mCherry foci traces over 100 min. Expanded images of boxed tracks (right). **f,** Median cumulative distance traveled by Rad52-mCherry foci. *P* calculated by two-tailed Mann-Whitney test; n=1120 foci from 13 nuclei (CK-689), 720 foci from 12 nuclei (CK-666). **g,** Mean square displacement (MSD) of Rad52-mCherry foci. Data shown as mean and weighted s.e.m.; n=3262 foci from 13 nuclei (CK-689), 2143 foci from 12 nuclei (CK-666). Δt=time interval. **h,** pEGFP-RPA32-NLS foci clustering in MTFs. **i,** RPA32-pEGFP-NLS foci traces over 100 min. **j,** Arpc2 protein levels in whole-cell lysates from Arpc2-LoxP-CreER MTFs (single experiment). **k,** Median cumulative distance traveled by RPA32-pEGFP-NLS foci. *P* calculated by one-way ANOVA with multiple comparisons; n=381 foci from 13 nuclei (CK-689), 370 foci from 12 nuclei (CK-666), 425 from 13 nuclei (4-OHT). **l,** RPA32-pEGFP-NLS foci MSD (Data shown as mean and weighted s.e.m.; n=790 foci from 13 nuclei (CK-689), 823 foci from 12 nuclei (CK-666), 1135 foci from 13 nuclei (4-OHT). Scale bar is 5 μm or as indicated.

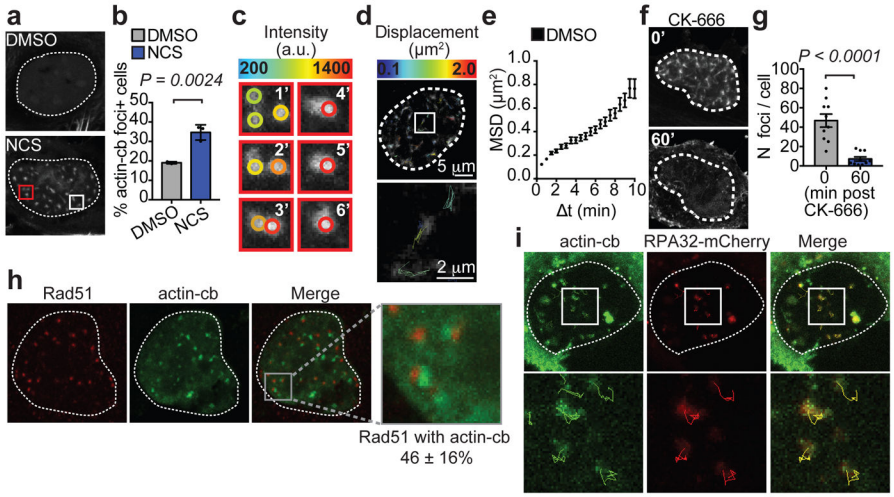

Figure 4. Nuclear actin foci cluster and localize to HDR sites

a, Representative images of U2OS nuclei transfected with nuclear actin-chromobody-tag-GFP (actin-cb). Boxes indicate clustering events. **b,** Percentage of actin-cb foci positive cells (*P* calculated by Student's two-tailed t-test; data shown as mean and s.d.; n=473 nuclei (DMSO), 473 nuclei (NCS). **c,** Expanded images of a clustering event from (**a,** red box). Circles denote foci intensity. **d,** Representative traces of actin-cb foci (out of 3 independent experiments) over 10 min. **e,** MSD of actin-cb foci (Data shown as mean and weighted s.e.m.; DMSO n=662 foci from 11 nuclei). **f,** Representative images of a U2OS nucleus with actin-cb foci following CK-666 treatment. **g,** Quantification of actin-cb foci prior to and post CK-666 treatment (*P* calculated by paired two-tailed t-test; data shown as mean and s.e.m.; n=10 nuclei from 2 independent experiments). **h,** Representative images of a U2OS nucleus showing Rad51 co-localization with actin-cb foci. The percentage of Rad51 foci that overlap or touch actin-cb foci shown (n=12 nuclei). **i,** Representative images of a U2OS nucleus (from five independent experiments) showing traces of RPA32-mCherry-NLS foci (red) and actin-cb foci (green). Scale bar is 5 μm or as shown.

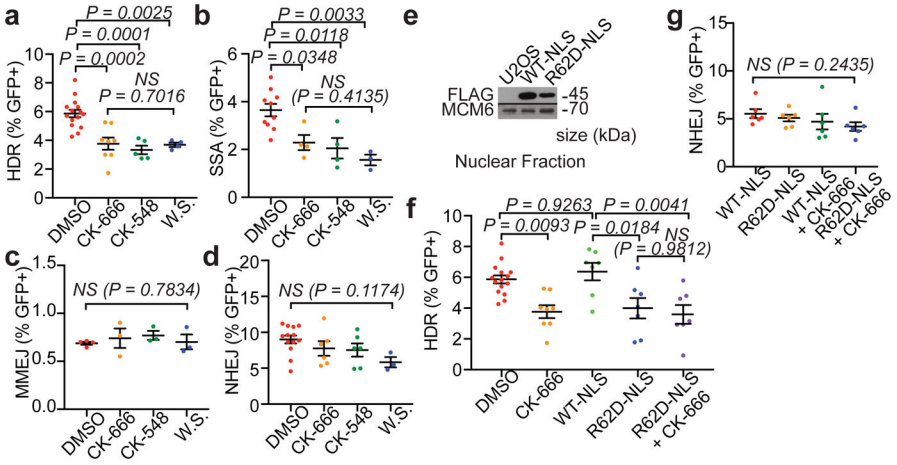

Figure 5. WASP and Arp2/3 mediate HDR

a, Summary of DR-GFP (HDR) assay (n=10, 6, 4, 4 left to right). ns, not significant. **b,** Summary of SA-GFP (SSA) assay (n=7, 4, 4, 3 left to right). **c,** Summary of EJ2-GFP (MMEJ) assay (n=4, 3, 3, 3, left to right). **d,** Summary of EJ5-GFP (NHEJ) assay (n=14, 6, 6, 3, left to right). **e,** Western blot shows FLAG-WT-NLS or FLAG-R62D-NLS overexpression in U2OS nuclear soluble fraction (single experiment). **f,** DR-GFP assay in cells transfected with FLAG-WT-NLS or FLAG-R62D-NLS. (n=7, 7, 7, left to right). HDR efficiency in the presence of DMSO or CK-666 (Fig. 5a) shown for comparison. **g,** EJ5-GFP assay in cells transfected with FLAG-WT-NLS or FLAG-R62D-NLS. (n=6, 6, 6, left to right). For **5a–g**, *P* calculated by one-way ANOVA with multiple comparisons as indicated; data shown as mean and s.e.m. n represents independent experiments.

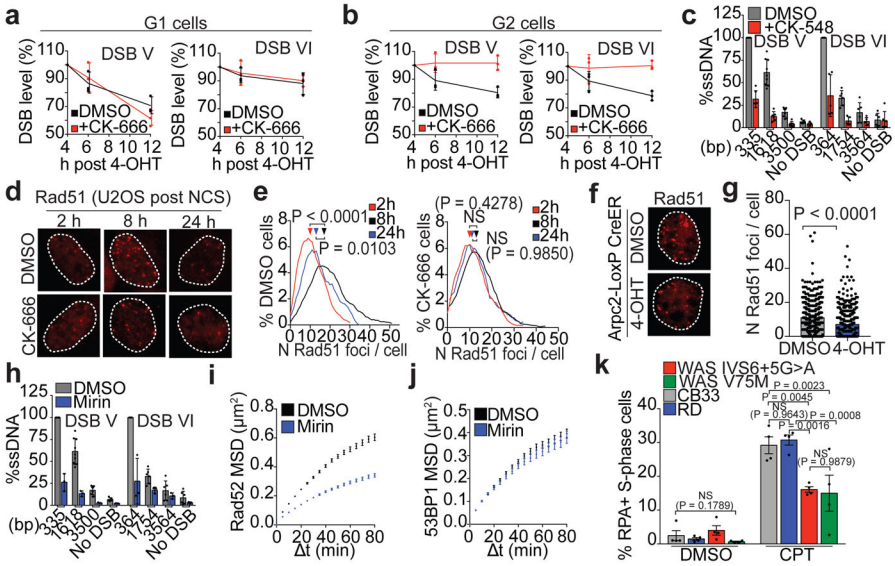

Figure 6. Arp2/3 facilitates resection and repair in G2

a, DSB repair at DSBs V-VI in G1-synchronized, ER-AsiSI-AID U2OS cells. Mean and s.d. (n=3 technical replicates) of a representative experiment shown. **b,** DSB repair at DSBs V-VI in G2-synchronized ER-AsiSI-AID U2OS cells. Mean and s.d. (n=3 technical replicates) of a representative experiment shown. **c,** Enrichment of single-stranded DNA (ssDNA) at DSBs V–VI following CK-548 treatment. (Data shown as mean and s.d., n=6 replicates from 2 independent experiments). **d,** Representative images of U2OS nuclei showing Rad51 foci. **e,** Quantification of Rad51 foci (*P* calculated by one-way ANOVA with multiple comparisons; smoothed traces show distribution of Rad51 foci. Arrow above respective curves indicates mean number of foci per cell; DMSO: 2 hours n=1830 cells, 8 hours n=2440 cells, 24 hours n=782 cells, CK-666: 2 hours n=2438 cells, 8 hours n=2189 cells, 24 hours n=912 cells). **f,** Representative images of Arpc2-LoxP-CreER MTF nuclei showing Rad51 foci. **g,** Quantification of Rad51 foci in MTFs (*P* calculated by two-tailed Mann-Whitney test; data shown as mean; n=571 nuclei (DMSO), 462 nuclei (4-OHT). **h,** Representative ssDNA enrichment at DSBs V–VI following mirin treatment. (Data shown as mean and s.d.; n=3 replicates of 2 independent experiments). ssDNA in DMSO-treated cells (Fig. 5c) shown for comparison. **i,** MSD of Rad52-mCherry foci (Data shown as mean and weighted s.e.m.; DMSO n=3292 foci from 12 cells, Mirin n=2677 foci from 11 cells). **j,** MSD of 53BP1-YFP foci in G1 cells (Data shown as mean and weighted s.e.m.; DMSO n=893 foci from 12 cells, Mirin n=744 foci from 14 cells). **k,** Quantification of chromatin-bound RPA in S-phase cells (*P* calculated by two-way ANOVA with multiple comparisons; data shown as mean and s.e.m.; n=4 independent experiments).